
Synthetic ground motions to support the Fennoscandian GMPEs

Ludovic Fülöp¹

Vilho Jussila¹

Billy Fälth²

Peter Voss³

Björn Lund⁴

¹ VTT Technical Research Centre of Finland Oy

² Claytech AB

³ Geological Survey of Denmark and Greenland (GEUS)

⁴ Uppsala University

Abstract

The relevance of near-field earthquakes to the safety of nuclear power plants (NPPs) in Fennoscandia is very high. De-aggregation from probabilistic seismic hazard assessment (PSHA) studies indicates that the prevailing source of hazard from ground accelerations of engineering interest is from mid-magnitude earthquakes at less than 50 km distance from the NPPs. Unfortunately, there are very few recordings of Fennoscandian earthquakes in the range of distances of this highest interest. We have developed a method to generate synthetic ground motions by physics-based modeling. Since the ground motion prediction (GMPE) is an essential part of PSHA computation we verify the simulation results with the G-16 GMPE (Graizer) developed for hard rock sites. The agreement between G-16 and our results is good at distances up to 30 km.

Key words

earthquake modeling, synthetic ground motions, probabilistic hazard assessment

Synthetic ground motions to support the Fennoscandian GMPEs

Final Report from the NKS-R SYNTAGMA (Contract: NKS-R(18)126/5)

Ludovic Fülöp¹, Vilho Jussila¹

Billy Fälth²

Peter Voss³

Björn Lund⁴

¹ VTT Technical Research Centre of Finland Oy, Finland

² Clay Technology AB, Sweden

³ Geological Survey of Denmark and Greenland (GEUS), Denmark

⁴ Uppsala University, Sweden

Table of contents

| | Page |
|---|------|
| 1. Introduction | 3 |
| 2. Modelled earthquake scenarios | 3 |
| 3. Modelling approach | 5 |
| 3.1 Dynamic rupture modelling | 5 |
| 3.1.1 Outcome of the dynamic rupture modelling | 10 |
| 3.2 Kinematic earthquake modelling | 11 |
| 4. Results | 14 |
| 4.1 Processing of the ground motions | 14 |
| 4.2 Generating response spectra | 15 |
| 4.3 Displacement ground motion results | 17 |
| 4.4 Spectra results and their comparison to ground motion prediction equations (GMPE) | 21 |
| 5. Conclusions | 28 |
| 6. Future prospects | 29 |
| 7. Acknowledgments | 29 |
| 8. Disclaimer | 29 |
| 9. References | 29 |

Appendix: Supporting information – Response spectra dataset in excel format. Available for download at [http://www.nks.org/download/nks-424_appendix - supporting information.xlsx](http://www.nks.org/download/nks-424_appendix_-_supporting_information.xlsx).

1 Introduction

In recent years earthquake source modelling methods have been developed, partly in earlier NKS projects (Fulop *et al.* 2016, 2017; Jussila *et al.* 2017), to substantiate the expected earthquake ground motion in Fennoscandia, in the ranges where empirical observations are not available. These ranges are the higher end of observed magnitudes, especially above ($M_w > 4.0$) and at distances closer than those available from instrumental recordings ($0 < d < 40 \text{ km}$). These ranges are very important contributor to the seismic hazard, with de-aggregation showing well above 50% of the seismic hazard contribution from this interval (Fülöp *et al.* 2015).

The practical way how decay of the ground motions is plugged into the probabilistic seismic hazard (PSHA) calculation is by the ground motion prediction equation (GMPE). GMPEs are predictors of the amplitudes of the ground motions with distance from earthquake sources with different characteristics (magnitude, focal mechanism, depth etc.). They are calibrated using empirical observations, ground motions, measured from real earthquakes. Obviously, if no empirical observation exists for a certain range of the earthquake source parameters (e.g. $M_w > 4$), the GMPE cannot be calibrated, or it has to be based on an extrapolation to the ranges where data is missing.

Synthetic ground motions, created in benchmark modelling within the NKS project AddGROUND, highlighted shortcomings of some currently used Fennoscandian ground motion equations and triggered the need to update these GMPEs (Jussila *et al.* 2017). In the present study (SYNTAGMA), we generate a larger set of synthetic ground motions with the intention of using available observations and the synthetic ground motions to support each other. We also intend to specifically create synthetic ground motions for magnitudes and distances where natural observations are unavailable in Fennoscandia, hence providing the GMPE developers with data.

In addition to the technical outcome, this project also aims at maintaining a network of experts focused on the diffuse seismicity areas of the Nordic Countries and further enhance the cooperation between Nordic partners in the area of earthquake source modelling. Using the modelling technique developed here, we explore and strengthen the interdisciplinary field between rock mechanics, seismology and earthquake engineering. Rock mechanics principles are used to model earthquake fault rupture scenarios in the deep underground. This work is very similar to work carried out for the nuclear waste companies Posiva and SKB, who are interested in predicting movements of faults and fractures. Seismology principles are used to define relevant earthquake scenarios, model the wave propagation to the ground surface and interpret if the obtained synthetic ground motions are plausible. Earthquake engineering principles are used to examine the synthetic ground motions from the hazard (PSHA) and risk (PRA) point of view. This area of probabilistic seismic hazard (PSHA) and seismic risk assessment (SPRA) are basic for increasing nuclear power plant safety.

2 Modelled earthquake scenarios

In this project, we generate ground motion results for 21 Fennoscandian earthquake scenarios in the magnitude range 4 – 5.5. As shown in Table 1, for the model catalogue we consider three focal depths (2, 10 and 20 km). The two largest depths correspond to depths that are

typically observed for earthquakes occurring in the Baltic shield (Bödvarsson *et al.*, 2006; Korja & Kosonen, 2015; Slunga, 1991). The hypocentre depth is gradually increased with magnitude, which is in line with both observation and expectable physical constrains.

There are observations also of much shallower events (Bödvarsson *et al.*, 2006), hence we include scenarios at 2 km hypocentre depth for the smallest magnitude events. A shallow earthquake is also relevant to include since it will generate strong surface ground motions and thus contribute significantly to the seismic hazard. These shallow events can be considered less common.

A stress drop of about 10 MPa is regarded as typical for intraplate conditions (Kanamori & Anderson, 1975). There are, however, notions of considerably higher stress drops in the Baltic Shield earthquakes (Slunga, 1991). Thus, we also include some scenarios with 50 MPa stress drop. As in the case of the shallow events, we consider the high stress drop earthquakes to be less common scenarios. However, research on small magnitude earthquakes in other stable continental regions is indicating that the stress-drop can be as high as 200 MPa (Onwuemeka *et al.*, 2018). Hence, the effect of stress-drop is a topic that will require a more systematic consideration in the future.

According to Slunga (1991) and Korja & Kosonen (2015), strike-slip earthquakes dominate in the Swedish part of the Baltic Shield. This is in accordance with the results of e.g. Lund & Zoback (1999) who inferred a strike-slip faulting stress regime at depth in the Siljan region in mid-Sweden. In Finland, however, a reverse faulting stress environment is more common at seismogenic depths (Korja & Kosonen, 2015; Uski *et al.*, 2003, 2006). In addition, there are stress measurements at shallow depths down to about 1 km in Forsmark, south-eastern Sweden (Glamheden *et al.*, 2007) and in Olkiluoto, south-western Finland (Posiva, 2011) that indicate a reverse faulting stress regime. In the suggested earthquake scenario catalogue in Table 1 we include reverse faulting, strike-slip faulting as well as oblique transpressive faulting mechanisms.

The earthquake ruptures we simulate are generic synthetic events that should be representative for intraplate conditions. The exact orientations of the faults are not important for the problem we address here. We simulate reverse and strike-slip faulting earthquakes on fault planes that are close to optimally oriented for slip relative to the stress field. For the reverse faulting (RF) events this means a fault with dip $\delta = 30^\circ$ (cf. Figure 1) and for the strike-slip (SS) events an almost vertical fault plane ($\delta = 80^\circ$). For the oblique transpressive faulting events we use a fault plane with $\delta = 45^\circ$. We set the rake angles (Figure 1) such that we avoid pure strike-slip and dip-slip direction movements on the fault plane. Hence, these models will provide intermediate cases compared to the benchmark models of the earlier NKS project (Fülöp *et al.* 2017).

Table 1. Targeted earthquake scenarios (“RF” = Reverse Faulting, “OB” = Oblique transpressive Faulting, “SS” = Strike-Slip Faulting)

| Focal depth (km) | Moment magnitude | Targeted focal mechanism | Stress drop (MPa) | Number of scenarios |
|------------------|------------------|--------------------------|-------------------|---------------------|
| 2 | 4 | RF, OB, SS | 10 | 3 |
| 10 | 4, 5, 5.5 | RF, OB, SS | 10 | 9 |
| 10 | 5.5 | RF, OB, SS | 50 | 3 |
| 20 | 5.5 | RF, OB, SS | 10, 50 | 6 |

3 Modelling approach

To build and run a numerical model that simulates a dynamic fault rupture as well as the propagation of the generated high frequency waves to distances tens of kilometres from the fault is computationally demanding. Such a model would need many tens of millions of elements for the discretization of the continuum and would be impractical to handle, especially if one wants to study several earthquake rupture scenarios. Thus, here we adopt the hybrid modelling approach that was used by Fülöp *et al.* (2017). The approach comprises two steps:

STEP 1 – Dynamic rupture modelling: A synthetic earthquake source is generated through numerical simulation of the fault rupture process. The fault slip temporal evolution is recorded at a large number of points on the fault plane. Then, linear time-slip functions are fitted to the recordings and used as input to the kinematic ground motion modelling in Step 2.

STEP 2 – Kinematic earthquake modelling: The linear time-slip functions determined in Step 1 are used as input to a kinematic earthquake modelling software, which is efficient for ground motion calculations. For a given earthquake source, and by assuming different depths for the fault, different ground motion scenarios can be generated.

3.1 Dynamic rupture modelling

We generate the earthquake source models by means of dynamic rupture modelling using the 3DEC software (Itasca 2013), which is a 3D modelling tool based on the distinct element method (Cundall 1971). 3DEC simulates the response of discontinuous media subjected to static or dynamic loading using an explicit time-stepping solution scheme. Joint planes can be kept active to model an assemblage of blocks or glued together to simulate a continuum. Blocks may behave either as rigid or deformable material. Deformable blocks are discretised using finite-difference elements and forces and relative movements along their boundaries are controlled by so-called subcontacts. 3DEC's capability to propagate waves properly has been verified by e.g. Fälth *et al.* (2015).

We simulate rupture scenarios generating different moment magnitudes, different focal mechanisms and different stress drops on fault planes with varying sizes (cf. Table 1). In all scenarios, the fault is planar, square-shaped and embedded in a finely discretized rock volume. We assume that the hypocentre is located in the middle of the fault (Figure 1). The dimensions of the rock volume are set large enough to prevent the boundaries from influencing the solution within the simulation time, which is set long enough that the slip has time to be completed over the entire fault plane. The discretization along the fault plane admits for proper transmission of 20 Hz waves. At larger distances the discretisation is made gradually coarser.

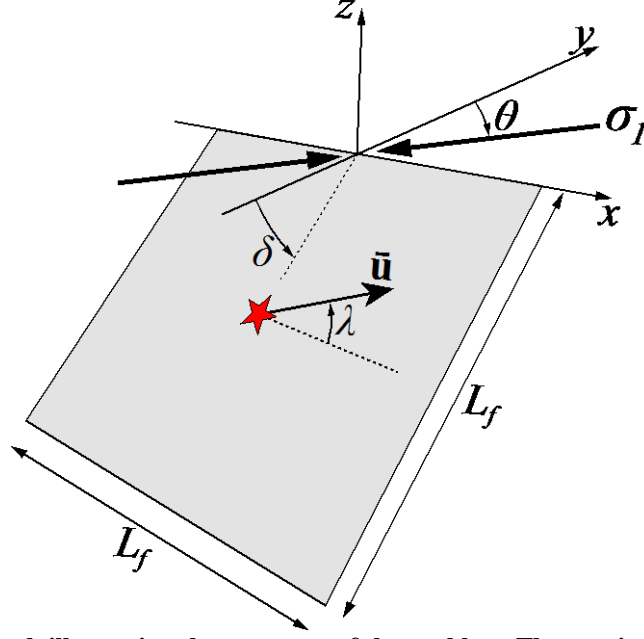


Figure 1. Schematic sketch illustrating the geometry of the problem. The star indicates the hypocentre in the middle of the square-shaped fault plane with edge length L_f . The angle δ is the dip of the fault plane relative to the horizontal while the trend of the major principal stress σ_1 is denoted θ . The initial stress field can be adjusted to obtain the desired rake angle λ of the fault slip vector \bar{u} .

The rock mass surrounding the fault plane is modelled as a linear elastic, homogeneous and isotropic continuum. In the kinematic ground motion calculations in Step 2, we adopt a layered velocity model of the crust that is typical for Nordic conditions (Table 4). Here in the 3DEC model, however, we simulate an earthquake rupture occurring on a fault that spans a limited depth range. Thus, we assume uniform mechanical properties, bulk modulus $K = 62$ GPa, shear modulus $G = 37$ GPa and density $\rho = 2875$ kg/m³. These properties correspond to about 10 km depth, given the adopted layered velocity model (Table 4), and yield seismic velocities of $V_p = 6.2$ km/s and $V_s = 3.6$ km/s.

To model the fault strength breakdown during dynamic rupture propagation, we adopt the commonly used linear slip-weakening law (Ida 1972), which means that the fault frictional coefficient is modelled as a linear function of fault slip u , i.e.

$$\mu^{sw} = \begin{cases} \mu_d + (\mu_s - \mu_d) \left(1 - \frac{u}{d_c}\right) & , u < d_c \\ \mu_d & , u \geq d_c \end{cases}, \quad (1)$$

where μ_s and μ_d are the ultimate (static) and the final (dynamic) friction coefficients, respectively, and d_c is slip-weakening distance.

The slip-weakening concept is illustrated in Figure 2a. As indicated in Figure 2b, the initial fault shear stress τ_{ini} is in-between the ultimate (static) and the final (dynamic) stresses τ_s and τ_d . The stress drop is defined as the change in fault shear stress during the earthquake, i.e. $\Delta\tau = \tau_{ini} - \tau_d$. To initiate the rupture, we adopt an approach described by Bizzarri (2010). Starting at the hypocentre we enforce a radially expanding rupture to propagate at a constant rupture speed $V_{force} = 0.5V_s$ within a nucleation region Σ_{nucl} according to

$$\mu^{TW} = \begin{cases} \mu_s - (\mu_s - \mu_d) \frac{(t - t_{force})}{t_0} & , t - t_{force} < t_0 \\ \mu_d & , t - t_{force} \geq t_0 \end{cases} \quad (2)$$

Here, Eq (2) is a time-weakening law, where the strength is ramped down linearly from μ_s to μ_d over a specified time t_0 . The time of rupture initiation at each location is denoted t_{force} . The friction coefficient at different positions (x, y, z) on the fault surface is determined by

$$\mu = \begin{cases} \min\{\mu^{SW}, \mu^{TW}\} & , \forall (x, y, z) \in \Sigma_{nucl} \\ \mu^{SW} & , \forall (x, y, z) \notin \Sigma_{nucl} \end{cases} \quad (3)$$

where μ^{SW} and μ^{TW} are determined by Eq. (1) and Eq. (2), respectively. At some time during the initiation process, when the ruptured area has grown large enough, the slip-weakening law (Eq. (1)) takes over and the rupture propagates spontaneously.

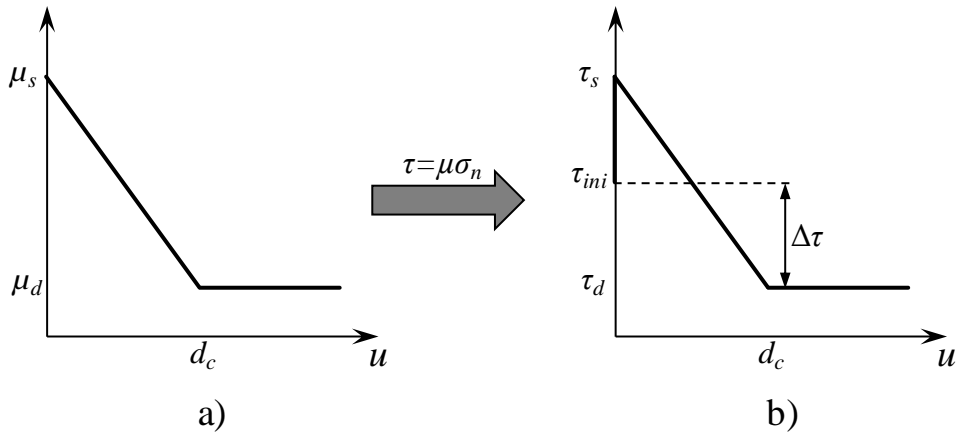


Figure 2. Linear slip-weakening law. (a) The fault frictional coefficient during spontaneous rupture propagation is modelled as a linear function of slip u . (b) For a given fault normal stress σ_n , the static and dynamic friction coefficients μ_s and μ_d correspond to the static and dynamic fault shear stress levels τ_s and τ_d , respectively. The initial shear stress τ_{ini} is in-between τ_s and τ_d . The stress drop is defined $\Delta\tau = \tau_{ini} - \tau_d$.

Data of stress magnitudes and stress orientations at depth are scarce. However, for this analysis where we create hypothetical rupture scenarios, it is not critical to have knowledge about the details of the stress field. There are, however, evidence indicating that the intraplate, continental upper crust is, in general and at some depth, in a state of frictional failure equilibrium on optimally oriented faults, see e.g. summary in Zoback and Townend (2001). We utilize stress fields that are constructed based on this assumption. For this we use the Mohr-Coulomb failure criterion, assuming frictional equilibrium on pre-existing, optimally oriented zones of weakness (e.g. Jaeger and Cook 1979):

$$\frac{\sigma_1 - P}{\sigma_3 - P} = \left(\sqrt{\mu^2 + 1} + \mu \right)^2 \quad (4)$$

Here, σ_1 and σ_3 are the major and minor principal stresses, respectively, while P is pore pressure and μ is the coefficient of friction. To constrain the intermediate principal stress σ_2 we use (after Gephart and Forsyth 1984)

$$R = \frac{\sigma_1 - \sigma_2}{\sigma_1 - \sigma_3} \quad (5)$$

We assume that the vertical stress σ_v is a principal stress and that it is a function of depth z and corresponds to the weight of the rock overburden, i.e. $\sigma_v = \rho gz$. Here, ρ is the density of the crust and g is the gravitational acceleration. Note that when determining σ_v , we assume the crust to be homogeneous, i.e. we assume ρ to be constant, in contradiction to the data reported in Table 4. By combining equations (4) and (5), we calculate the stress magnitudes in a strike-slip stress field (for use in strike-slip (SS) rupture scenarios) according to

$$\begin{aligned} \sigma_1 &= A(\sigma_3 - P) + P \\ \sigma_2 &= \sigma_v \\ \sigma_3 &= \frac{\sigma_2 - P(1-A)(1-R)}{A(1-R) + R} \end{aligned} \quad (6)$$

with $A = \left(\sqrt{\mu^2 + 1} + \mu \right)^2$

Similarly, we calculate the stresses in a reverse stress field (for reverse (RF) and oblique transpressive (OB) rupture scenarios) according to:

$$\begin{aligned} \sigma_1 &= A(\sigma_3 - P) + P \\ \sigma_2 &= \sigma_1(1-R) + \sigma_3 R \\ \sigma_3 &= \sigma_v \end{aligned} \quad (7)$$

When determining the stress field, we assume $\rho = 2875 \text{ kg/m}^3$, hydrostatic pore pressure P and $\mu = 0.6$. In all rupture scenarios we assume that the stresses correspond to a depth of 10 km, which means that $\sigma_v = 282 \text{ MPa}$. This is of course a simplification since we assume different depths for the events in the kinematic simulations in modelling step two. However, the important thing here is the stress drop $\Delta\tau$ that is generated during the earthquake, which for given fault dimensions, determines the amount of fault slip and thereby the moment magnitude of the earthquake. For a given fault dip angle δ , we adjust the trend θ of the major principal stress σ_1 and the stress ratio R (Eq. (5)) to obtain the desired rake angle λ of the fault slip vector $\bar{\mathbf{u}}$ (Figure 1).

The desired stress drop $\Delta\tau$ is obtained by adjustment of the fault dynamic friction coefficient μ_d . Then, the static friction coefficient μ_s and the slip-weakening distance d_c are set to get a stable rupture evolution. The model input parameters are summarised in Table 2.

Recall that we consider three types of faulting mechanisms, reverse faulting (RF), oblique transpressive faulting (OB) and strike-slip faulting (SS). In the reverse faulting scenarios, we set the fault dip $\delta = 30^\circ$ and adjust the stress field to arrive at rake angle $\lambda = 80^\circ$. The corresponding numbers for the oblique faulting scenarios are $\delta = 45^\circ$ and $\lambda = 45^\circ$, and for

strike-slip faulting $\delta = 80^\circ$ and $\lambda = 10^\circ$. Then, in order to simulate rupture scenarios that generate different moment magnitudes and stress drops, we combine the three faulting mechanisms with four fault areas. This gives twelve rupture scenarios, as shown in Table 2. With scenario #1 - #3 the intention is to generate earthquakes with a moment magnitude of about $M_w \sim 4$. With scenario #4 - #6 we aim at $M_w \sim 5$ and with scenario #7 - #12 we intend to generate $M_w \sim 5.5$ earthquakes. For scenario #1 - #9 we aim at a stress drop of 10 MPa and for scenario #10 - #12 we aim at 50 MPa. Note that for scenario #10 - #12, the fault area is smaller than the area in scenario #7 - #9 even though the intended moment magnitude is the same. This is because of the higher stress drop in scenario #10 - #12.

The fault area/stress drop trade-off is reported for the $M_w=5.0$ and 5.2 earthquakes in the Kaliningrad district, Russia on September 21, 2004. The earthquakes, causing moderate damage in Russia, Poland and Lithuania, are reported to have identical and exceptionally small source areas and are distinguished only by the stress drop, estimated to 24.6 MPa and 37.4 MPa for the two events respectively (Gregersen *et al* 2004).

Table 2. Model input parameters (RF = Reverse Faulting, OB = Oblique Faulting, SS = Strike-slip Faulting)

| Scenario | Mechanism* | Fault edge length L_f (km) | Fault dip δ (deg) | Stress field parameters | | d_c | μ_s | μ_d |
|----------|------------|------------------------------|--------------------------|-------------------------|----------|-------|---------|---------|
| | | | | R | θ | | | |
| 1 | RF | 1.0 | 30 | 0.5 | 18 | 0.022 | 0.620 | 0.560 |
| 2 | SS | | 80 | 0.9 | 40 | 0.022 | 0.500 | 0.445 |
| 3 | OB | | 45 | 0.8 | 47 | 0.022 | 0.565 | 0.500 |
| 4 | RF | 2.0 | 30 | 0.5 | 18 | 0.030 | 0.620 | 0.555 |
| 5 | SS | | 80 | 0.9 | 40 | 0.030 | 0.500 | 0.445 |
| 6 | OB | | 45 | 0.8 | 47 | 0.030 | 0.565 | 0.500 |
| 7 | RF | 3.5 | 30 | 0.5 | 18 | 0.050 | 0.620 | 0.555 |
| 8 | SS | | 80 | 0.9 | 40 | 0.050 | 0.500 | 0.445 |
| 9 | OB | | 45 | 0.8 | 47 | 0.050 | 0.565 | 0.500 |
| 10 | RF | 2.5 | 30 | 0.5 | 18 | 0.18 | 0.793 | 0.443 |
| 11 | SS | | 80 | 0.9 | 40 | 0.18 | 0.639 | 0.353 |
| 12 | OB | | 45 | 0.8 | 47 | 0.18 | 0.722 | 0.396 |

The 3DEC modelling was extended with a method to identify stress-states in the rock volume that will result in an instantaneous rupture in the planned direction. Hence, we are able to use 3DEC for generating free rupture in any random direction (rake and dip angle) allowing modelling of more realistic ruptures, adjusted to the observed fault plane solutions in Fennoscandia. This is a major update compare to earlier projects, where we were constrained to generate pure strike and dip slip ruptures.

3.1.1 Outcome of the dynamic rupture modelling

To illustrate how different earthquake source parameters are distributed over the fault plane we show in Figure 3 result from scenario #12. This scenario generates an oblique slip with rake $\lambda = 45^\circ$ on a fault with dip $\delta = 45^\circ$. We see in Figure 3a how the rupture is initiated at the fault centre. First, it propagates at a low speed, but accelerates when the slip-weakening law takes over. Note that the rupture accelerates quicker in the direction of slip (mode II shear)

(see the slip vector in Figure 3c) than in the perpendicular direction (mode III shear). On the other hand, the slip velocity tends to be lower along the direction of slip (Figure 3b). These phenomena are general features exhibited by fault ruptures and are caused by the interplay between the P- and S-waves that are generated by the rupture. In the direction of slip, both P- and S-waves work together to load the fault at the rupture front and thereby drive the rupture. In the direction perpendicular to slip only S-waves drive the rupture. These features, which have been observed also by others (e.g. Bizzarri 2012), are similar in all the rupture scenarios.

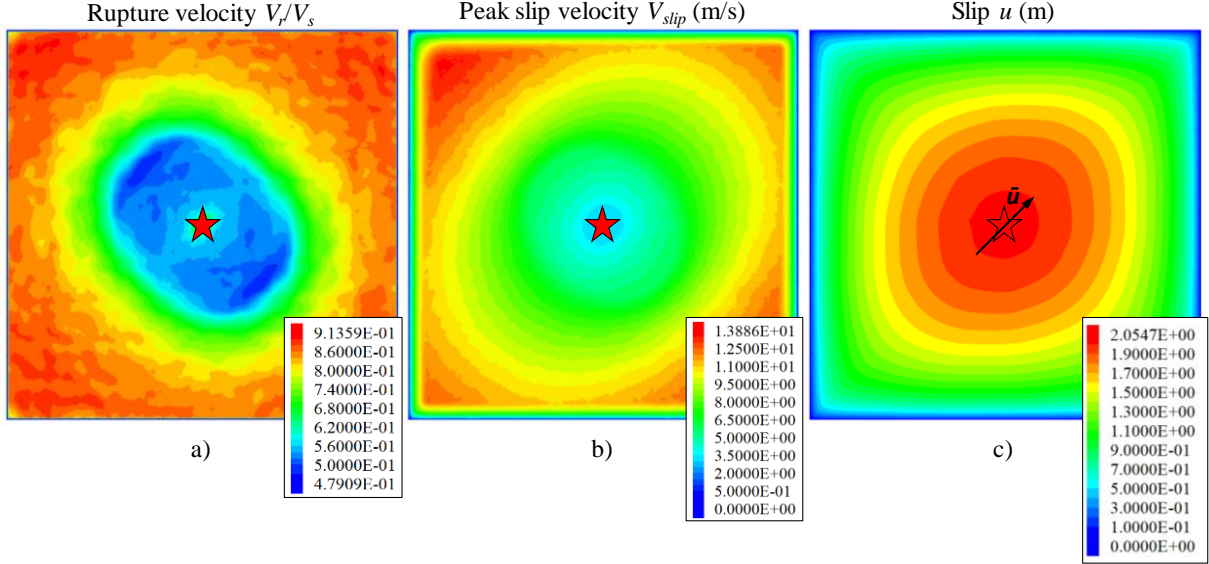


Figure 3. Results from scenario #12. a) Rupture propagation velocity V_r normalised to the shear wave velocity of the rock mass V_s , b) peak slip velocity V_{slip} and c) slip u . The arrow indicates the slip direction. The stars indicate the hypocentre.

A summary of the source parameters for the twelve rupture scenarios is presented in Table 3. A couple of things are worth to note:

- The moment magnitudes and stress drops are not exactly the intended ones. Particularly, the moment magnitudes of scenario #1 – #3 differ from the intended one (M_w 4.3 instead of M_w 4.0). This is because of the interplay between fault area, stress drop and fault slip (i.e. seismic moment, Eq. (8)). To construct the model such that the intended moment magnitude and stress drop are generated precisely, may lead to an extensive testing that includes several model runs with different model geometries and parameter settings. Since replicating the intended moment magnitude precisely was not critical for the purpose of this work, we limited the number of test runs and accepted some deviation from the intended numbers.
- Due to the much higher stress drops in scenario #10 – #12, these scenarios generate significantly higher fault slip velocities than the other scenarios.

To calculate the moment magnitude, we first calculate the seismic moment, as

$$M_0 = \bar{u}A_rG \quad \text{Nm}, \quad (8)$$

where \bar{u} , A_r and G are average fault slip, rupture area and rock mass shear modulus, respectively. Since the fault rupture propagates until it reaches the edges of the pre-defined fault surface, the rupture area is equal to the pre-defined fault area. Based on the seismic moment, the moment magnitude is calculated as (cf. Hanks and Kanamori 1979)

$$M_w = \frac{2}{3} \log_{10} M_0 - 6.07. \quad (9)$$

Table 3. Source parameters resulting for the modelled fault ruptures (RF = Reverse Faulting, OB = Oblique Faulting, SS = Strike-slip Faulting)

| # | Mechanism * | M_w | M_0 (Nm) | Stress drop $\Delta\tau$ (MPa) | Peak slip vel. V_{slip} (m/s) | Rupture area (km ²) | δ (deg) | λ (deg) | Number of source patches |
|----|-------------|-------|-------------------------------|--------------------------------|---------------------------------|---------------------------------|----------------|-----------------|--------------------------|
| 1 | RF | 4.3 | $3.9 \cdot 10^1$ ₅ | 9.7 | 1.7 | 1.0×1.0 | 30 | 80 | 324 |
| 2 | SS | 4.3 | $4.0 \cdot 10^1$ ₅ | 9.9 | 1.7 | | 80 | 9.9 | |
| 3 | OB | 4.3 | $3.8 \cdot 10^1$ ₅ | 9.5 | 1.7 | | 45 | 46 | |
| 4 | RF | 5.0 | $3.5 \cdot 10^1$ ₆ | 10 | 2.7 | 2.0×2.0 | 30 | 80 | 1156 |
| 5 | SS | 5.0 | $3.4 \cdot 10^1$ ₆ | 10 | 2.6 | | 80 | 9.8 | |
| 6 | OB | 5.0 | $3.4 \cdot 10^1$ ₆ | 10 | 2.7 | | 45 | 45 | |
| 7 | RF | 5.5 | $2.0 \cdot 10^1$ ₇ | 12 | 3.8 | 3.5×3.5 | 30 | 80 | 3364 |
| 8 | SS | 5.4 | $1.8 \cdot 10^1$ ₇ | 11 | 3.5 | | 80 | 9.8 | |
| 9 | OB | 5.4 | $1.8 \cdot 10^1$ ₇ | 11 | 3.7 | | 45 | 46 | |
| 10 | RF | 5.6 | $3.0 \cdot 10^1$ ₇ | 50 | 14 | 2.5×2.5 | 30 | 80 | 1764 |
| 11 | SS | 5.6 | $3.0 \cdot 10^1$ ₇ | 48 | 13 | | 80 | 9.9 | |
| 12 | OB | 5.6 | $2.9 \cdot 10^1$ ₇ | 50 | 14 | | 45 | 46 | |

3.2 Kinematic earthquake modelling

To determine input to the second modelling step, we use the method described in Fülöp *et al.* (2017). We record the fault slip at a grid of recording points on the 3DEC fault plane and fit linear time-slip functions in the strike-slip and dip-slip directions to these recordings. The grid spacing is 62.5 m. From this, we obtain slip function parameters for the corresponding grid of sub-faults in Compsyn software (Spudich & Xu, 2003)

Compsyn first computes Green's functions for wave propagation in the frequency domain. The computation uses Discrete Wavenumber/Finite Element (DWFE) method by Olson *et al.* (1984). It uses reciprocity relations, which enables effective and simultaneous computation of the wave motion for all source – observer combinations. The number of elements required depends on the highest wavenumber. Since the number of elements are independent of the Earth structure, it could be complicated but in practice, the Earth is presented as horizontal layers in Compsyn. The material parameters for each layer are elastic and the thickness should

be much greater than the considered wavelengths. The modelling technique requires an artificial boundary deep enough to prevent reflections of unwanted waveforms in the synthetic waveform. As can be seen in Table 4, the bottom boundary is at 42 km, which is similar the depth of the Moho discontinuity in Fennoscandia (Grad 2009).

The Compsyn package is divided into five separate executables. Three of them are responsible for the calculations and two are writing processes. The first executable takes care of setting the bottom boundary and the creation of the Finite Element mesh and stiffness matrices. A time step algorithm transforms the time series into the frequency domain. The second executable computes traction surfaces for the user defined fault plane. In our experience, this is the most time consuming process since all run-time information is written on a hard drive. The third and last executable reads the traction surfaces and integrates the dot products of the tractions with the kinematic slip model defined by the user. Finally, the ground motions in terms of displacement and velocity are transformed back to the time domain. The accelerations must be calculated afterwards in the time domain since the integration in the frequency domain is problematic when the frequency is zero.

The fault plane is divided into hundreds of small patches (Table 3). Each of them is an individual point source, which emits waves to the surface of the Earth. The main input for the computation of synthetic ground motions with Compsyn are the layered Earth model (Table 4), strike and dip slip rates, rise times and rupture times for each fault patch. Since 3DEC provides slip, the slip rates are computed in a separate procedure. The reason for using slip rates instead of slip is that the slip rate behaves better in the frequency domain (Spudich & Archuleta, 1987). Rise time is the time required to develop the slip, i.e. the duration of slip of each individual patch, while strike and dip slip rates control the movement direction of the patch. The rupture time describes the starting moment of the slip on each patch from the moment of initiation of the rupture in the hypocentre. Rupture time is shortest for the patches that are closer to the hypocentre, gradually increasing for patches further away from the hypocentre. Spudich and Archuleta (1987) discussed the role of slip rate, rise time and rupture time. Their conclusion was that a change in the slip rate or rise time have a small, while changes of rupture time have more noticeable influence on synthetic ground motions.

The computation process of ground motions can easily be divided into separate processes due to the reciprocity relation of the Green's function. In practice, the Green's function is computed only once but it can be reused for computing ground motions at multiple observation points. Multiple CPUs can be used if the observation grid (Figure 4) on the Earth surface is clustered in groups. Each group is submitted separately to Compsyn. Once the groups are running simultaneously, they occupy individual CPUs and reduce the total computation time.

Table 4. Depth to layer, P-wave and S-wave velocity and density of the layered Earth model.

| Layer number | Depth (km) | P-Wave velocity (km/s) | S-Wave velocity (km/s) | Density (g/cm ³) |
|--------------|------------|------------------------|------------------------|------------------------------|
| 1 | 0.0 | 5.30 | 3.10 | 2.65 |
| 2 | 0.8 | 5.80 | 3.30 | 2.72 |
| 3 | 15.0 | 6.45 | 3.75 | 3.02 |
| 4 | 42.0 | 6.89 | 3.90 | 3.07 |

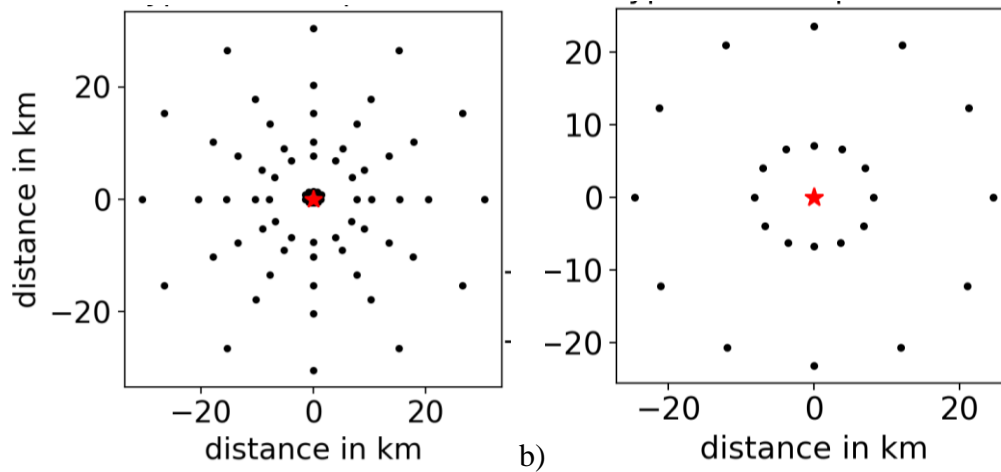


Figure 4. Example of observation points indicated by the black dots on the Earth surface when the hypocentre depth is 2.0 km (a) and 20.0 km (b). The red star indicates the epicentre. The angular coordinate varies by 30.0° interval beginning from 0.0° and ending to 330.0°. In (a), the rupture distances are 2.0, 7.5, 15.0, 20.0 and 30.0 km. In the subplot (b), the rupture distances are 20.0 and 30.0 km.

The outcomes of the fault rupture models from 3DEC are merged with the earthquake modelling cases intended in Table 1, resulting in the twenty-one earthquake modelling cases given in Table 5.

Table 5. Earthquake scenarios modelled in Compsyn (“RF” = Reverse Faulting, “OB” = Oblique Faulting, “SS” = Strike-Slip Faulting)

| Case | Hypocentre depth (km) | Mechanism * | Moment magnitude (M_w) | Seismic moment | Average Stress drop (MPa) | Average slip (m) | Peak slip velocity (m/s) | Rupture area (km^2) | Dip | Rake |
|------|-----------------------|-------------|----------------------------|---------------------|---------------------------|------------------|--------------------------|--------------------------------|-----|------|
| 1 | 2 | RF | 4.3 | $3.9 \cdot 10^{15}$ | 9.7 | 0.11 | 1.7 | 1 | 30 | 80 |
| 2 | 10 | | | | | | | | | |
| 3 | 2 | SS | 4.3 | $4.0 \cdot 10^{15}$ | 9.9 | 0.11 | 1.7 | 1 | 80 | 9.9 |
| 4 | 10 | | | | | | | | | |
| 5 | 2 | OB | 4.3 | $3.8 \cdot 10^{15}$ | 9.5 | 0.11 | 1.7 | 1 | 45 | 46 |
| 6 | 10 | | | | | | | | | |
| 7 | 10 | RF | 5.0 | $3.5 \cdot 10^{16}$ | 10 | 0.24 | 2.7 | 4.0 | 30 | 80 |
| 8 | 10 | SS | 5.0 | $3.4 \cdot 10^{16}$ | 10 | 0.23 | 2.6 | 4.0 | 80 | 9.8 |
| 9 | 10 | OB | 5.0 | $3.4 \cdot 10^{16}$ | 10 | 0.23 | 2.7 | 4.0 | 45 | 45 |
| 10 | 10 | RF | 5.5 | $2.0 \cdot 10^{17}$ | 12 | 0.45 | 3.8 | 12.3 | 30 | 80 |
| 11 | 20 | | | | | | | | | |
| 12 | 10 | SS | 5.4 | $1.8 \cdot 10^{17}$ | 11 | 0.41 | 3.5 | 12.3 | 80 | 9.8 |
| 13 | 20 | | | | | | | | | |
| 14 | 10 | OB | 5.4 | $1.8 \cdot 10^{17}$ | 11 | 0.41 | 3.7 | 12.3 | 45 | 46 |
| 15 | 20 | | | | | | | | | |
| 16 | 10 | RF | 5.6 | $3.0 \cdot 10^{17}$ | 50 | 1.3 | 14 | 6.3 | 30 | 80 |
| 17 | 20 | | | | | | | | | |
| 18 | 10 | SS | 5.6 | $3.0 \cdot 10^{17}$ | 48 | 1.3 | 13 | 6.3 | 80 | 9.9 |
| 19 | 20 | | | | | | | | | |
| 20 | 10 | OB | 5.6 | $2.9 \cdot 10^{17}$ | 50 | 1.3 | 14 | 6.3 | 45 | 46 |
| 21 | 20 | | | | | | | | | |

4 Results

We generate two types of model outputs from the hybrid model: (1) displacement ground motion in a dense grid of points and (2) spectral results at selected points of output corresponding to equal rupture distances (R_{rup}) from the fault plane.

4.1 Processing of the ground motions

In each observation point on the ground surface we output the ground displacement evolution with time, in the global X-Y-Z-system (Z is vertical direction), and from them we calculate the corresponding velocity and acceleration signals. For the displacement ground motion output like in Figure 9, we generate the rotated displacement signals in the radial (R) and tangential (T) direction from the epicentre at each output point. We similarly rotate the velocity and acceleration signals.

The rotation procedure is exemplified below for Case 9, a simulated earthquake of moment magnitude 5.0, oblique focal mechanism, and hypocentre depth 10 km. The position of the observer is $X=-12$ km on the horizontal axis and $Y=7$ km on the vertical axis Figure 5a.

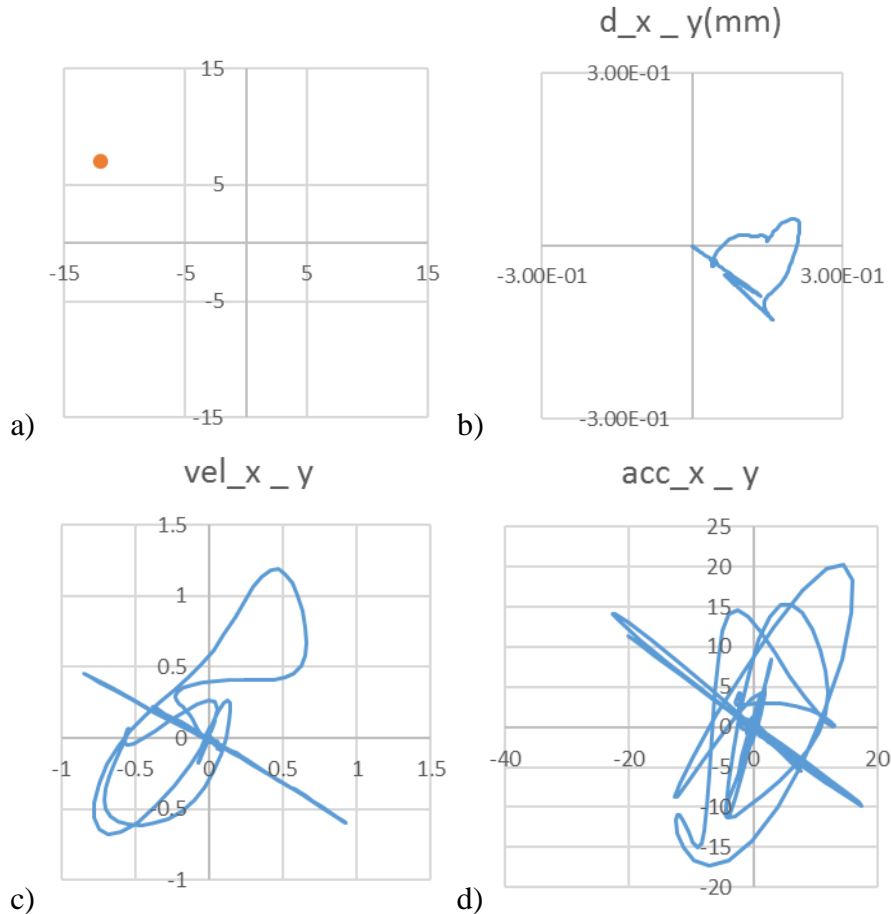


Figure 5. (a) Position of the observation point on ground surface at coordinates -12, 7 from the epicentre and plots of the horizontal particle motion for (b) displacement, (c) velocity and (d) acceleration in the observation point. Units are mm, mm/s and mm/s² respectively.

In the models the faults always strike parallel to the X axis direction. The horizontal components of the ground motion in the observation point are given in Figure 5b, c and d as particle motion in terms of displacement, velocity and acceleration, respectively, in the X-Y

coordinate system. The motion plotted in Figure 5 are the complete 16s long wave train in the observation point. The accelerations are the same as the ones in Figure 6 and Figure 7, where they are represented as two individual components. Figure 5 show linear polarisation of the first part of the wave field, oriented toward (for other observation points away), from the source. This polarization is the reason for rotating to R and T components, as it creates a basis for easy inspection of the wave-field is in line with the expectations from the theory.

We plot the time series of the X and Y components of acceleration in Figure 6. It can be noted that both components have P- and S-wave parts. However, unlike natural ground motions, synthetic recordings have no noise and they have no features dependent on wave scattering (e.g. Coda waves, etc.). They are only the direct waves propagating from the earthquake fault to the observation point.

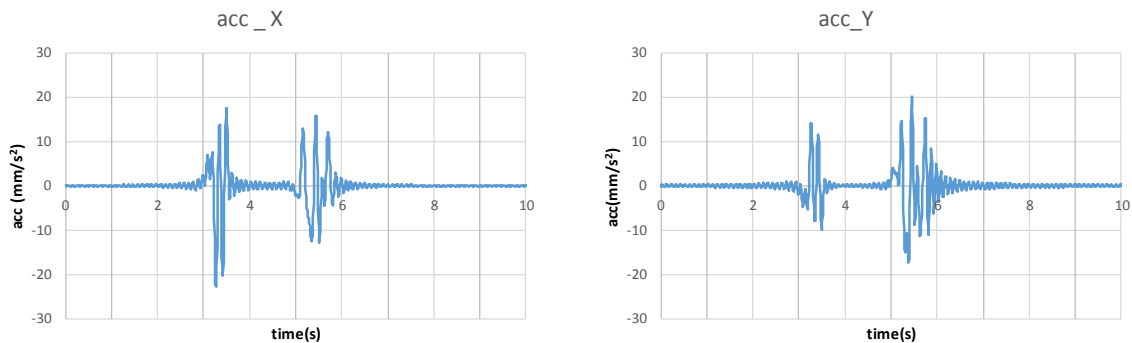


Figure 6. Horizontal components of the acceleration in the observation point at coordinates (-12km, 7km)

We then rotate the X and Y component ground motions to radial (R) and transverse (T) directions relative to the epicentre. This rotation better emphasises the P- and S- components as seen in Figure 7. The better separation is occurring with accelerations, velocities and displacements alike. We plot R and T displacement components in map views like in Figure 11, because they are most useful for assessing the wave patterns emerging from the different faults. We use ground motions with a frequency content of up to 10 Hz for generating areal plots.

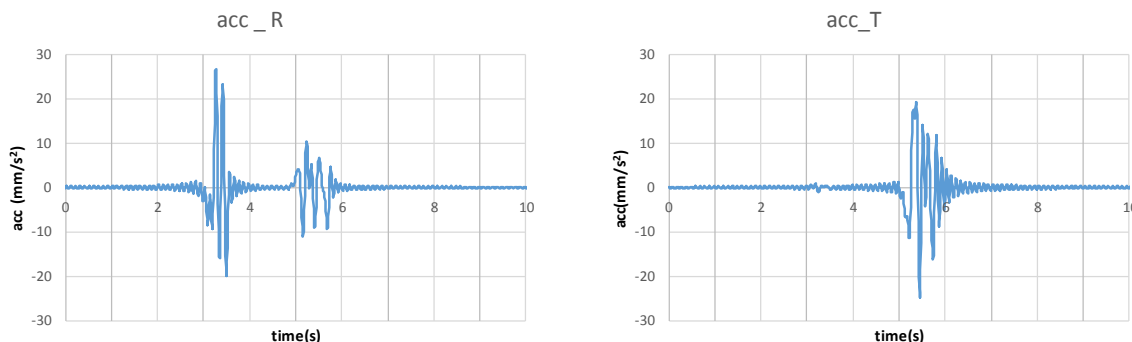


Figure 7. Rotated radial (left) and transverse (right) components of the acceleration in the observation point at coordinates (-12 km, 7 km).

4.2 Generating response spectra

A processed output of the hybrid models is response spectra. In order to create such spectra, we extract ground motions in a less dense grid than for map view plots, but with a frequency

content of up to 25 Hz. We calculate the rotated acceleration components from 0 to 360 degrees with a step of 1 degree, from the X and Y acceleration signals. This procedure is equivalent to virtually rotating the seismometer at the observation point with steps of 1 degree. To each rotation angle, the rotated accelerogram is used to calculate the response spectrum. The outcome is a set of 360 response spectra between the frequencies of 0.1-100 Hz.

For each frequency within the spectra the median value is picked from within the 360 spectral ordinates. This spectral ordinate has 50% probability of being exceeded with different instrument orientations. The procedure produces a mean spectrum (RotD50) introduced by Boore (2010), eliminating the influence of the seismometer alignment. We present results in RotD50 spectra in this report instead of the traditional geometric mean (GM) spectra. To highlight the difference, the GM spectrum calculation procedure is described below.

To obtain a GM spectrum, we first calculate the acceleration response spectra from the original X and Y acceleration components resulting in two spectra in the 0.1-100 Hz frequency range. In the next step, the geometric mean of the spectral ordinate is calculated for each frequency. The outcome is another type of mean spectrum (GM spectrum) for each observation point.

While almost equivalent to the RotD50 spectrum, the shortcoming of the GM spectrum is that it is dependent on the orientation of the X and Y measuring directions. The GM spectrum depends on how the seismometer is oriented in the field.

The outcome of the RotD50 and GM calculation procedures for an observation points at angular coordinate 60 degree and rupture distance 15 km, is shown in Figure 8a and b. The GM and RotD50 spectra are not that different from each other. It can also be noticed that the rotated spectra in the RotD50 procedure provide a maximum and minimum envelope of the possible spectra at the observation point. These envelopes are covering the X and Y direction measurements, however both the minimum and the maximum envelope only correspond to a single orientation out of the 360 orientations calculated. Hence, these extremes have very small probability of realization. It is also worth noting that the envelopes are not necessary single spectra resulting from a unique orientation. It can be that at 50 Hz in the spectra it is a certain orientation that produces the maximum spectral response, while at 5 Hz it is a different orientation.

We would also note that the trends, seen in Figure 8 between the GM and RotD50 spectra are not universal. Here we can notice a $PGA_{RotD50} \sim PGA_{GM}$ and spectra amplification slightly higher in the RotD50 spectra at $\sim 0.47g$ compare to $\sim 0.41g$ for the GM spectra. However, these trends are unique to this particular case.

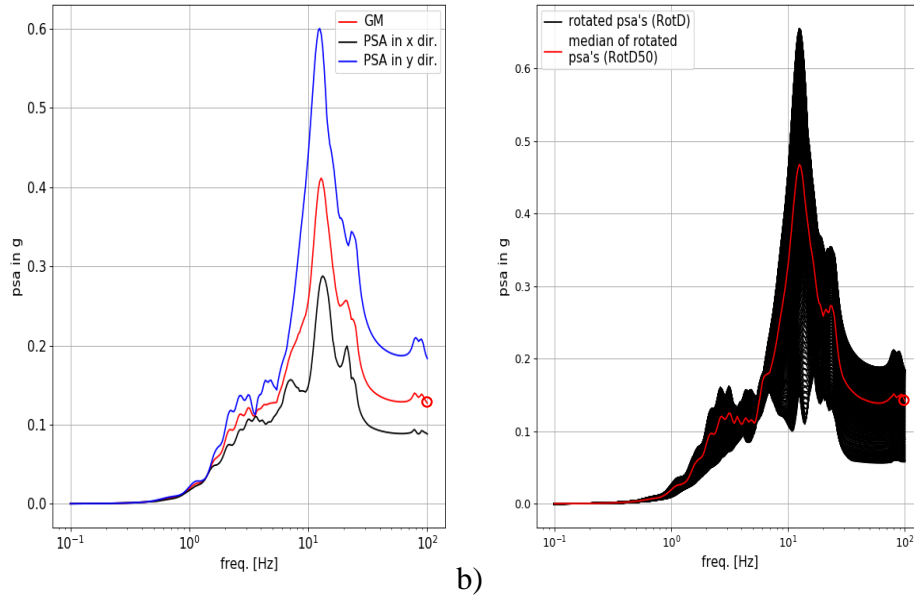


Figure 8. (a) Acceleration spectra (SA) in X and Y direction at angular coordinate 60 deg and rupture distance 15 km are shown with black and blue solid lines respectively. Geometric mean (GM) of the PSAs is shown with red solid line. The moment magnitude is $M_w=5.0$. (b) Plot of the 360 individual rotated spectra is plotted with black and the RotD50 median, corresponding to 50% probability, with red. The red circles at 100Hz indicate the PGA in the two cases.

In summary, the RotD50 and GM spectra both intend to represent the average effect of the ground motion on the observation point. They are about equivalent. The RotD50 spectra is slightly more advanced, because it eliminates the effect of the instrument orientation from the averaging procedure. Hence, independently of the instrument orientation, we would obtain the same RotD50 spectra, but the GM spectra would depend on the orientation of the instrument. The error of the GM procedure is significant in strongly polarised recordings where one of the signals is very small (e.g. $X \sim 0$). In those cases, when calculating the geometric mean, the very small component would make the GM also almost zero.

In the annexed data to this report, we summarise the X, Y, Z, the GM, RotD50 and RotD100 spectra. We only use the RotD50 spectra for comparisons in the report, partly because it is generally superior to GM, but also particularly because synthetic ground motions are more prone to show strong polarization compared to instrumental recordings. The 100 Hz RotD50 spectral ordinate is referred to as peak ground acceleration (PGA) in this report.

4.3 Displacement ground motion results

First, we plot the displacement fields at the ground surface for the different earthquake scenarios. In order to do this, we create a dense grid of output points within an area of 40×40 km around the epicentre. Because generating ground motion output in a dense grid with high frequency content is computationally expensive, we use only a representation of the ground motion with content up to 10 Hz. We extract the ground displacement components R, T and Z at to generate the surface plots. These plots help visualise the wave propagation pattern and are an instrument to assess the quality of the wave pattern for the modelled scenario.

Figure 9, Figure 10 and Figure 11 present three example cases of the oblique (OF), reverse (RF) and strike slip (SS) faulting, respectively. The cases we call RF and SS in this work are not pure reverse and strike-slip cases. As it can be noted in Table 3, the rake angle (λ) is 80

degrees for the RF. Hence, our RF fault movement has a small strike direction components because of the $90-80=10$ degree inclination. Similarly, the SS faults do not follow pure strike slip moment, since the rake angle is $\lambda=9.8-9.9$ degrees, resulting in a small dip direction movement of the fault. This deviation from pure RF and pure SS explains the asymmetries in Figure 10 and Figure 11.

Without going to a lengthy explanation of the wave patterns, we highlight the following features that are indicative to the different faulting types. In case of oblique faulting (OF), both the dip and rake angles are about 45 degrees. Hence, in a vertical projection like in Figure 9, the overall movement of the fault plan is oblique with angle <45 degrees. The wave patterns reflect this movement (e.g. 5.9s transversal component in Figure 9). The wave pattern also indicate a movement away from the source in the $-X, +Y$ quadrant (e.g. 4.1-5.9s radial component in Figure 9) and movement towards the source in the other quadrants. These observations of the ground surface movement are consistent with the OF used.

Similarly, Figure 10 shows a consistent ground motion pattern with the RF used. For instance, the 3.9s time radial displacement frame in Figure 10 shows a movement away from the source in the $-Y$ half and a movement towards the source in the $+Y$ half. The vertical movement in the entire RF area is up (3.9s vertical in Figure 10) and there is a slight $-X, +X$ asymmetry due to the 10degree strike direction movements. Again, we find the ground motion pattern consistent with the RF fault movement.

Finally, Figure 11 is showing a typical SS ground motion field of four lobes, slightly disturbed by the 9.8 degree dip direction movement in that fault rupture scenario. We find that ground motion patterns for all the cases are consistent with the modelled fault movements.

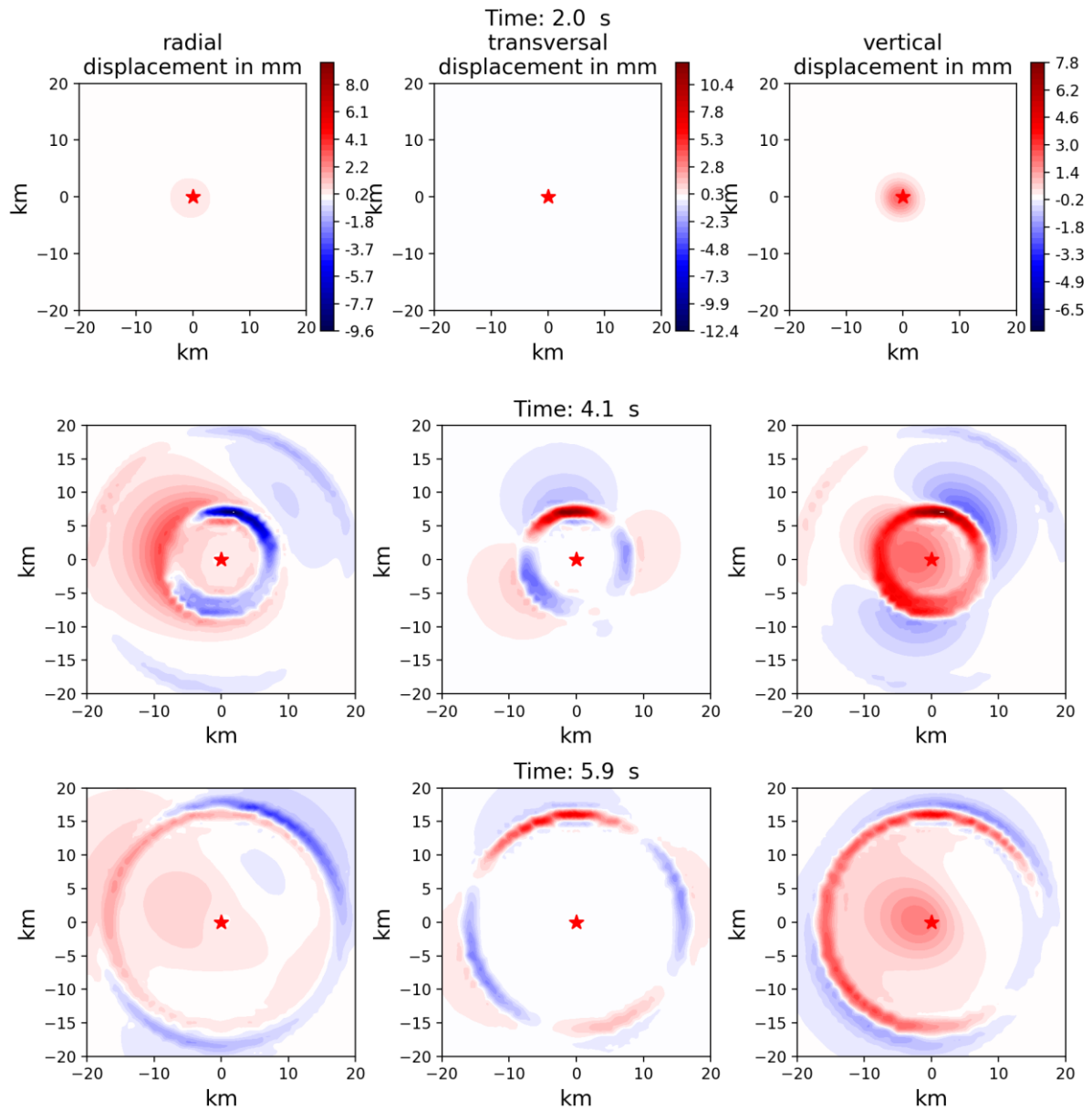


Figure 9. Displacements (mm) on the ground surface from an $M_w=5.0$ earthquake, occurring on a fault dipping 45 degrees, in case of oblique transpressive faulting; Case 6 in Table 3. Strike direction is horizontal direction (X-axis), while dip direction is along the positive (Y-axis). The rows in the figure are time slices at 2, 4.1 and 5.9 s. The columns in the figure are the radial, transverse and vertical components of the displacement. The depth of the hypocentre is 10 km.

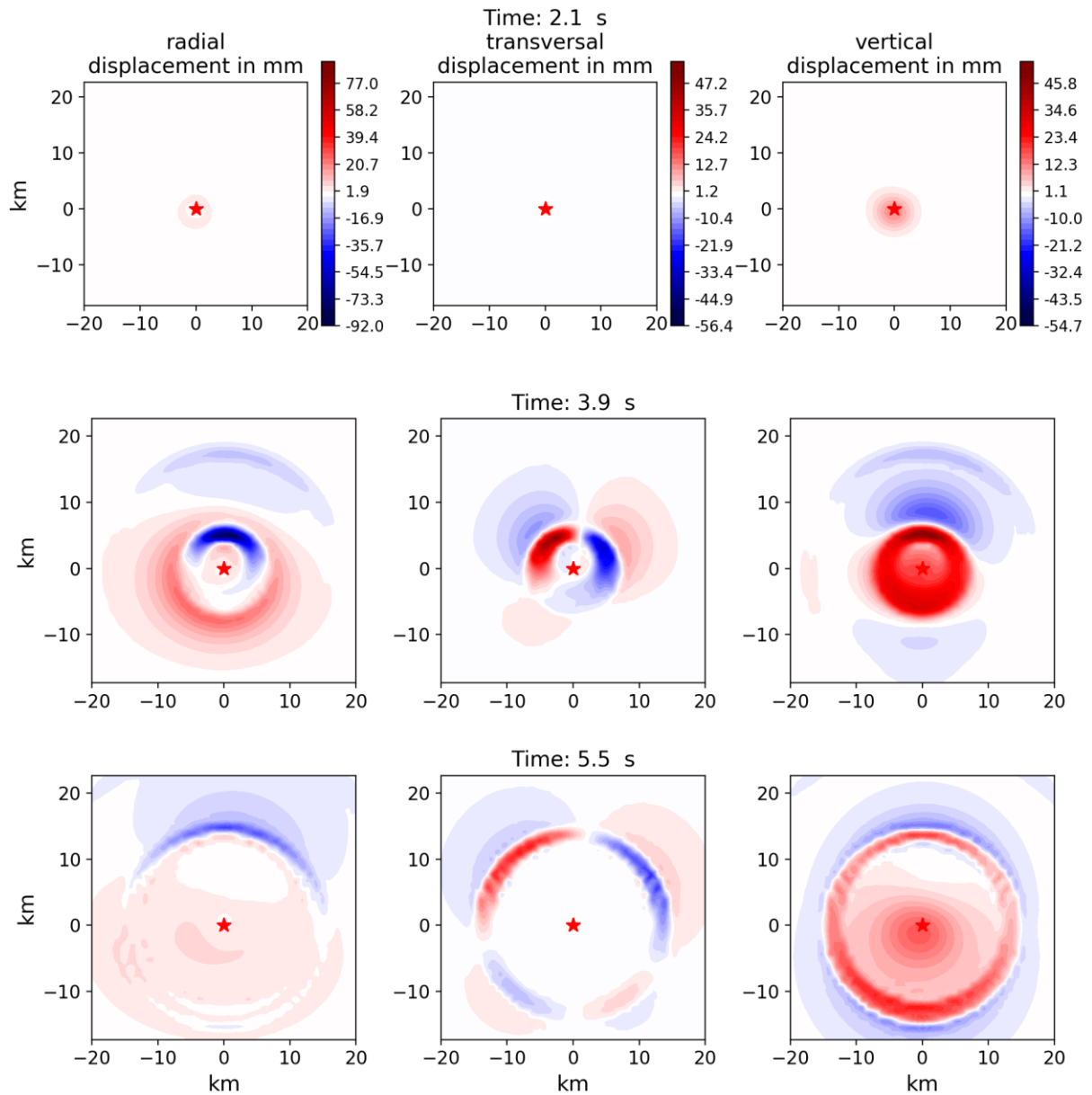


Figure 10. Displacements (mm) on the ground surface from an $M_w=5.6$ earthquake, occurring on a fault dipping 30 degrees, in case of reverse faulting, Case 10 in Table 3. Strike direction is horizontal direction (X-axis), while dip direction is along the positive (Y-axis). The rows in the figure are time slices at 2.1, 3.9 and 5.5 s. The columns in the figure are the radial from epicentre, transverse and vertical components of the displacement. The depth of the hypocentre is 10 km.

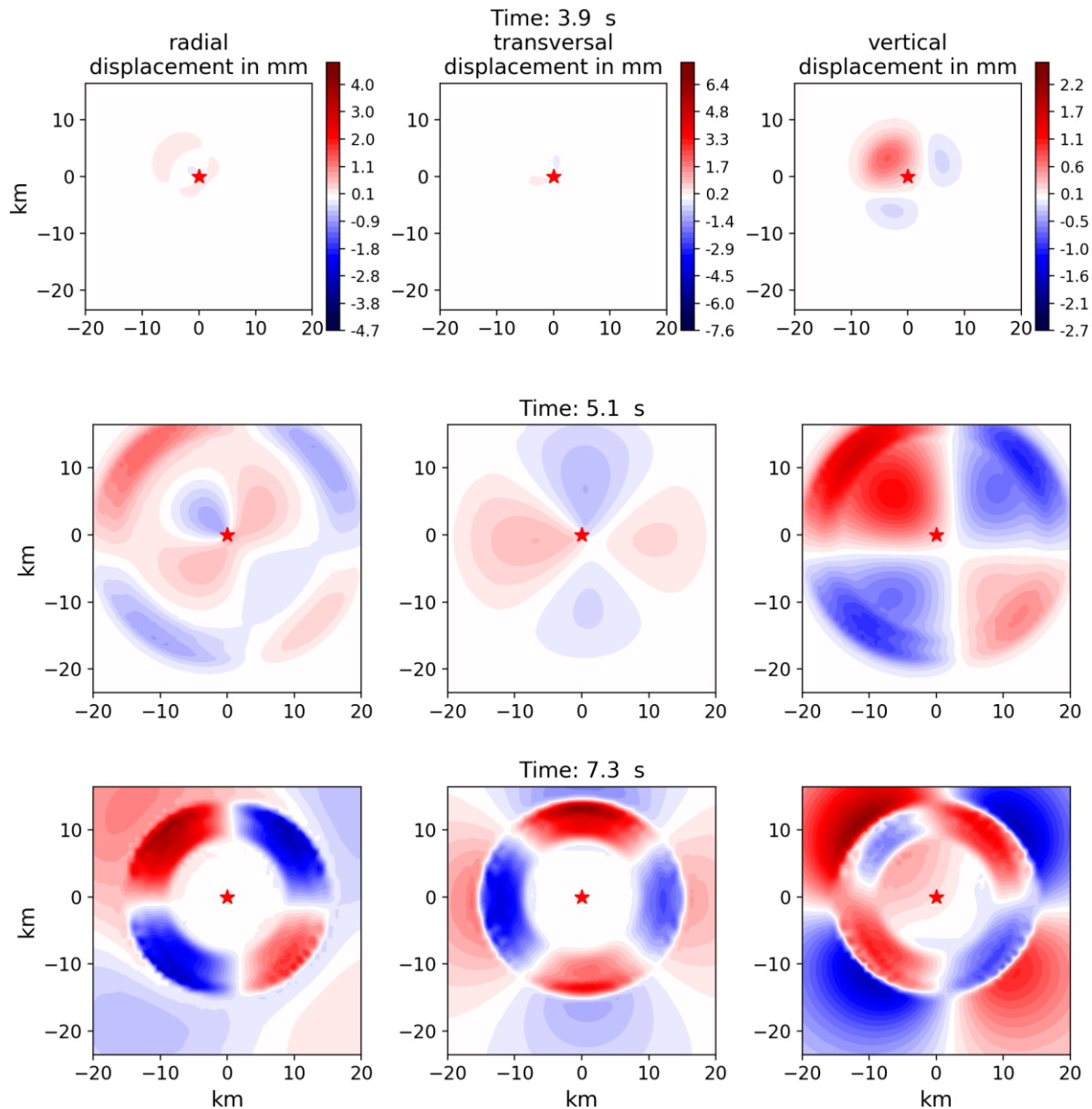


Figure 11. Displacements (mm) on the ground surface from an $M_w=5.4$ earthquake, occurring on a fault dipping 80 degrees, in case of strike slip; Case 8 in Table 3. Strike direction is horizontal direction (X-axis), while dip direction is along the positive (Y-axis). The rows in the figure are time slices at 3.9, 5.1 and 7.3 s. The columns in the figure are the radial from epicentre, transverse and vertical components of the displacement. The depth of the hypocentre is 20 km.

4.4 Spectral results and their comparison to ground motion prediction equations (GMPE)

First, we present the horizontal PGA values for the modelling cases thought to be more representative to Fennoscandian seismicity from the point of view of depth and stress drop (Figure 12). Concerning the depth, we only have two recent events in Fennoscandia close to the magnitude $M_w 4.3$. These are the Bothnia bay earthquake of 2016, with $M_L 4.1$ and a hypocentre depth of 21.6km, and the Sveg earthquake of 2014 with $M_L 4.2$ and a depth estimate of 6.2km. Hence, the $M_w 4.3$ at ~10km depth is more supported by observation than the 2km depth case; and a stress drop of about 10 MPa is regarded typical for intraplate events (Kanamori & Anderson, 1975).

The individual predictions of PGA at equal rupture distances (R_{rup}) are shown with orange dots. These dots correspond to observation points at equal rupture distance, but at different orientations relative to the fault (Figure 4). The plots aggregate all faulting types (RF, OF and SS) and different depths in the case of the M_w 5 and M_w 5.5 earthquakes. There is a large scatter, of about one order of magnitude, in PGA at the same R_{hyp} . This scatter relate to azimuth, faulting mechanism and depth. However, it is usual in ground motion prediction that the biases to these parameters are not explicitly separated. The median value for each distance is shown with a red horizontal line.

As basis for comparison to the synthetic data, we choose the ground motion prediction equation (GMPE) G-16 developed by Graizer (2016). The G-16 GMPE was developed for stable continental regions (SCR) and for very hard rock conditions of shear wave velocity up to $V_{s30}=2800$ m/s. This is close to our shear wave velocity of $V_{s30}=3100$ m/s used in the crustal model (Table 4). We consider the difference to be of minor importance for such stiff soil conditions.

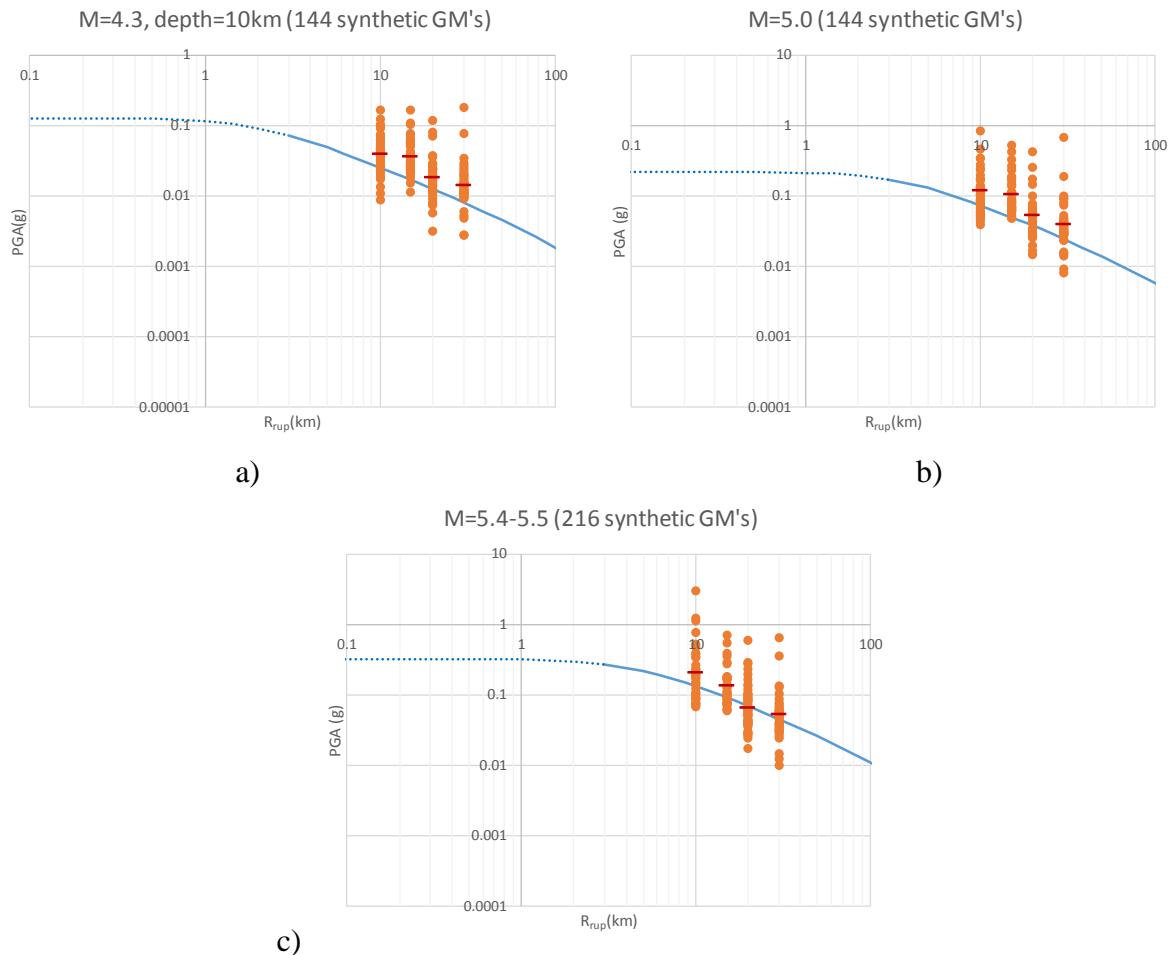


Figure 12. PGA values from the synthetic ground motions for rupture distances of 10, 15, 20 and 30 km. Orange points correspond to PGA from (a) $M_w=4.3$, (b) $M_w=5$ and (c) $M_w=5.4-5.5$ magnitude earthquakes. In (a) only the 4.3 event with hypocentre depth of 10 km is plotted. In (c) the 10 MPa stress-drop cases are shown. Types of faulting (OF, SS, RF) are not distinguished. Red lines are the median PGA for each R_{rup} . The blue line is the PGA prediction of the G-16 GMPE for hard-rock sites of $V_{s30}=2800$ m/s (Graizer, 2016).

Since G-16 has been developed using data from the eastern US and south-eastern Canada (Goulet *et al.* 2014), it can be argued that the GMPEs prediction is relevant for Fennoscandia. Canadian data has earlier been used to substantiate safety studies for nuclear power plants in Finland (Varpasuo *et al.*, 2001).

The median values align well, but slightly exceed the PGA prediction of the G-16 GMPE (blue line). The validity of the GMPE is up to shear wave velocity $V_{s30}=2800$ m/s, and this is the value used for the plots in Figure 12. Quantifying the difference between our synthetic data and the GMPE predictions suggest that our median PGA are 45% higher within the target distance range of this work (<30km). Test showed that additional model optimization is required to determine PGA values beyond 30 km.

Exploring the statistical distribution of the PGA values at each distance range, we note that logarithmic distribution is adequate to describe them. For instance, Figure 13 presents the PGA distribution from the $M_w=5.4-5.5$ earthquake cases with hypocentre depth at 10 and 20 km.

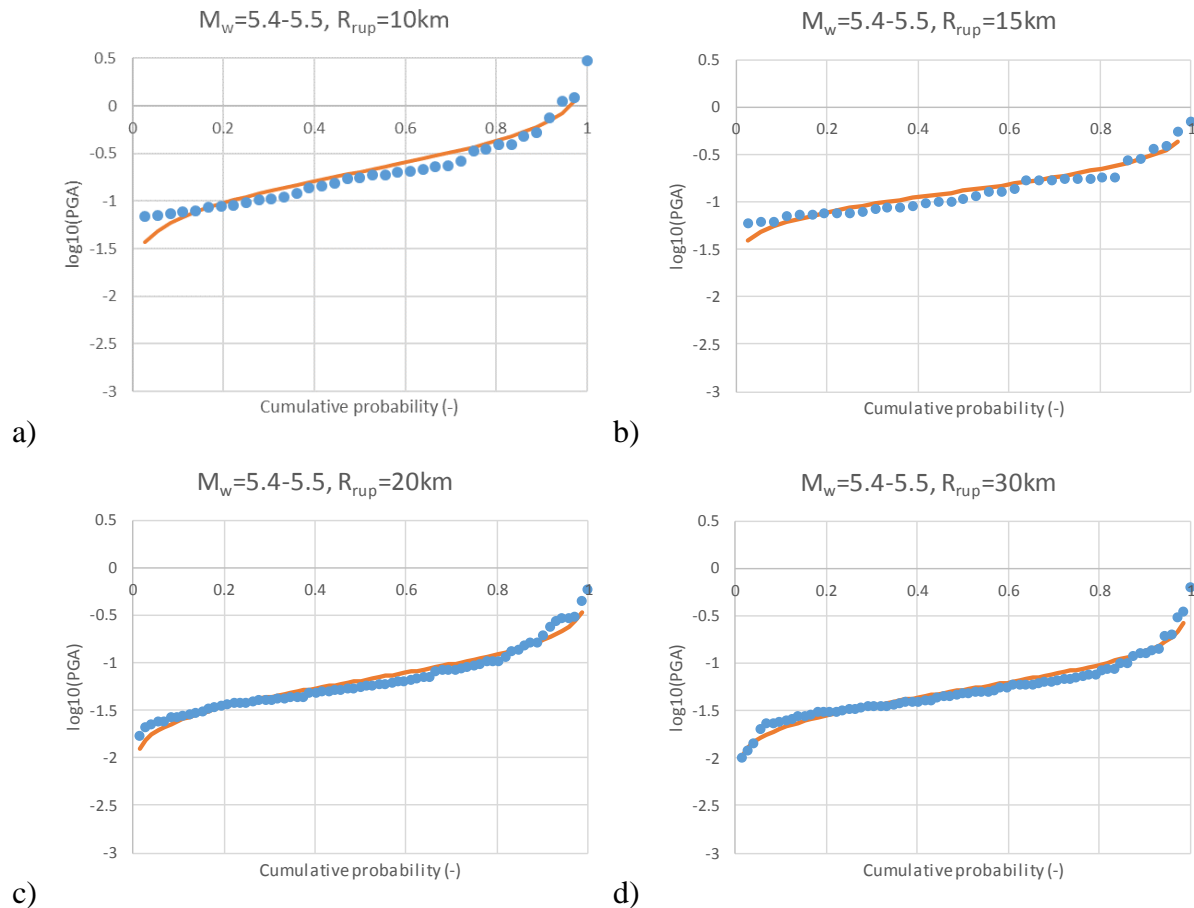


Figure 13. Distribution of the PGAs at different rupture distances for the $M_w=5.4-5.5$ earthquakes with stress drop 10 MPa. There are two hypocentre depths, $D_{hypo}=10$ km and 20 km. The 20 km case does not have observation points at $R_{rup}=10$ km and 15 km, since the closest ground surface distances exceeds these values. Hence, (a) and (b) only contains points from the shallower earthquake. The orange lines are normal distributions fitted to the 10th base logarithm of the PGA.

The parameters of the fitted normal distribution to $\log_{10}(\text{PGA})$ of each modelled scenario is shown in Table 6, with the mean and the standard deviation of $\log_{10}(\text{PGA})$. The two $M_w=4.3$ scenarios are given separately for the 2 km and 10 km depth cases and for both cases together.

Table 6. Parameters of the normal distribution fitted to $\log_{10}(\text{PGA})$ of the synthetic ground motions

| Moment magnitude (M_w) | Hypocentre depth (km) | $R_{rup}=2$ km | | $R_{rup}=7.5$ km | | $R_{rup}=10$ km | | $R_{rup}=15$ km | | $R_{rup}=20$ km | | $R_{rup}=30$ km | |
|----------------------------|-----------------------|----------------|------|------------------|------|-----------------|------|-----------------|------|-----------------|------|-----------------|------|
| | | Mean | Std. | Mean | Std. | Mean | Std. | Mean | Std. | Mean | Std. | Mean | Std. |
| 4.3 | 2 | -0.43 | 0.29 | -1.16 | 0.33 | -1.33 | 0.35 | -1.56 | 0.34 | -1.71 | 0.34 | -1.90 | 0.35 |
| 4.3 | 10 | - | - | - | - | -1.40 | 0.29 | -1.45 | 0.26 | -1.75 | 0.31 | -1.86 | 0.34 |
| 4.3 | 2, 10 | -0.43 | 0.29 | -1.16 | 0.33 | -1.37 | 0.32 | -1.51 | 0.30 | -1.73 | 0.33 | -1.88 | 0.34 |
| 5 | 10 | - | - | - | - | -0.93 | 0.30 | -0.99 | 0.27 | -1.29 | 0.31 | -1.42 | 0.35 |
| 5.4-5.5 | 10, 20 | - | - | - | - | -0.69 | 0.39 | -0.88 | 0.27 | -1.19 | 0.33 | -1.28 | 0.32 |
| 5.6 | 10, 20 | - | - | - | - | -0.28 | 0.32 | -0.41 | 0.27 | -0.70 | 0.30 | -0.80 | 0.33 |

The $M_w=4.3$, 2 km depth event and the $M_w=5.6$ event with stress drop 50 MPa are characterised by increased ground motion PGA (Table 6). We anticipated this effect at the design of the modelling program, as explained in earlier sections of the report. We present comparison of these two cases, with the ones believed to be more typical scenarios for Fennoscandia. In Figure 14 the comparison of the PGA dataset for the two hypocentre depths of the $M_w=4.3$ earthquake are given.

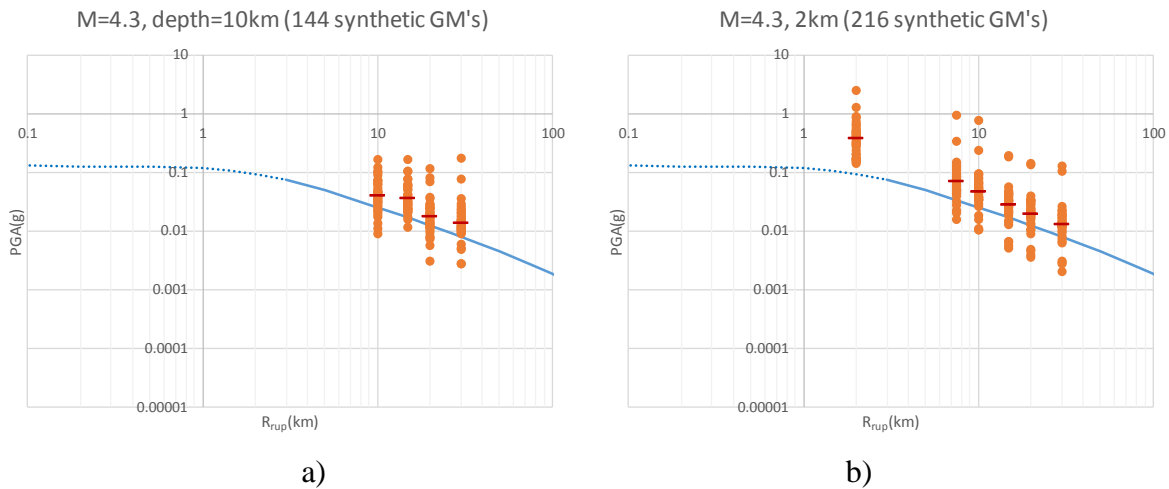


Figure 14. Comparison of the $M_w=4.3$ earthquakes with different depth. The orange dots are the individual PGA at different azimuth; the red thick line is the median, blue lines are the G16 prediction, which are equal to the two scenarios. For the 10km depth case, our closes R_{rup} is 10km, while for the shallower case we plot also the $R_{rup}=2$ km and 5km points.

We show the difference between the $M_w=5.4-5.5$ and the $M_w=5.6$ earthquakes in Figure 15. The intention at the outset of modelling was to have all ruptures at $M_w=5.5$. However, as explained earlier, mechanical properties and stresses are controlling the ruptures of the 3DEC models and moment magnitudes are outcomes of a spontaneous rupture process. Hence, in 3DEC we are not controlling the quantities leading to moment magnitude directly. As a result, some variation of the moment magnitude (M_w) is present in the modelled cases.

We assume that the $M_w=5.4-5.5$ cases are one dataset, resulting from stress drop of 10 MPa on the faults. Even if the $M_w=5.6$ earthquakes are compatible with the $M_w=5.4-5.5$ earthquakes in terms of magnitude; they are result of fault ruptures with larger stress drop (50 MPa) and smaller fault area. Traditional GMPEs would not distinguish between the two sets of data, because the two magnitudes are very close. However, the case with increased stress drop generates PGA values that considerably exceed those given by the GMPE at all rupture distances (Figure 15b), while the PGAs are only slightly above the GMPE with the 10 MPa stress-drop earthquakes (Figure 15a).

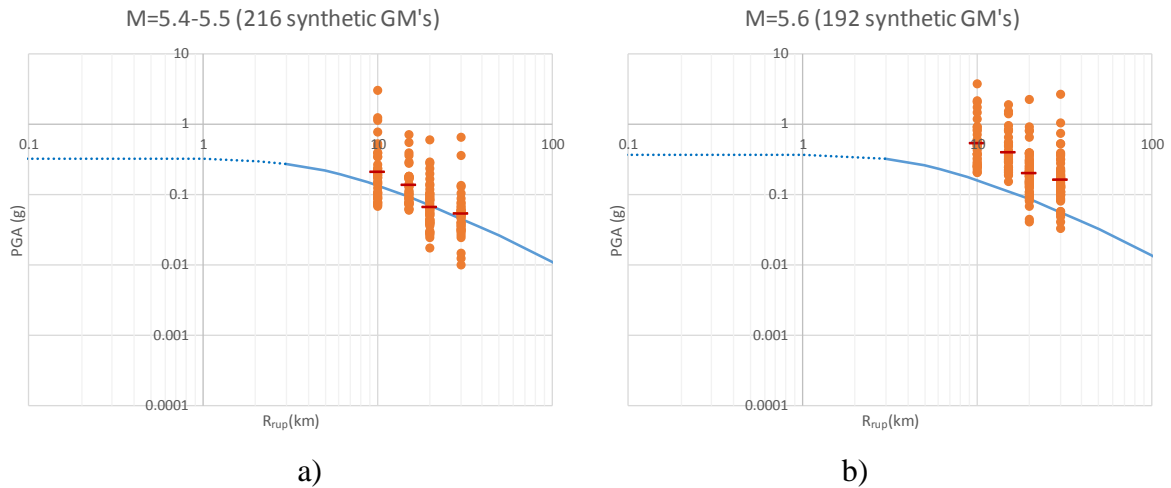


Figure 15. Comparison of the $M_w=5.4-5.5$ and $M_w=5.6$ earthquakes. Magnitudes are similar but the stress-drops are significantly different (10 MPa and 50 MPa). The blue lines are the G-16 prediction for 5.45 magnitude and 5.6 respectively. The orange dots are the individual PGA at different azimuth; the red thick line is the median PGA.

Both the hypocentre depth and stress drop comparisons above highlight the need to strictly scrutinise ground motion data used in GMPE development in Fennoscandia. Due to the lack of local strong motion data, ground motions from geologically similar regions are often adopted for Fennoscandia. In fact, this is what we do also when we compare with the G-16 GMPE, which is not locally calibrated. What Figure 14 and Figure 15 show, is that we need to prioritize GMPEs and earthquakes from similar depth and fault ruptures with compatible stress-drop.

Finally, we give the comparison of the spectra for the earthquake cases that we asses are more common (Figure 16, Figure 17, Figure 18) and for the cases that we consider to be more exceptional in terms of either depth or stress drop (Figure 19, Figure 20). The models were calibrated such that the ground motion is complete up to about 25 Hz. If we compare this to real measurements, this is equivalent to about 50-62.5 Hz sampling of measured signals. In terms of spectral results, the pattern observed at PGA are repeated.

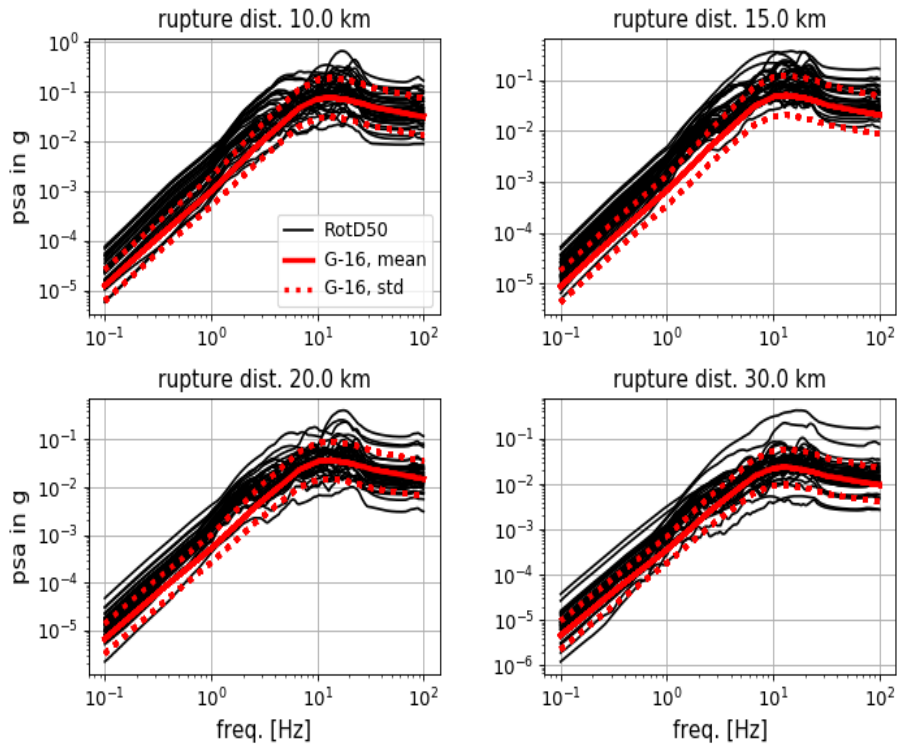


Figure 16. Comparison of spectra in black computed from the simulated ground-motion and the G-16 GMPE in red. The plot corresponds to $M_w=4.3$, hypocentre depth 10 km.

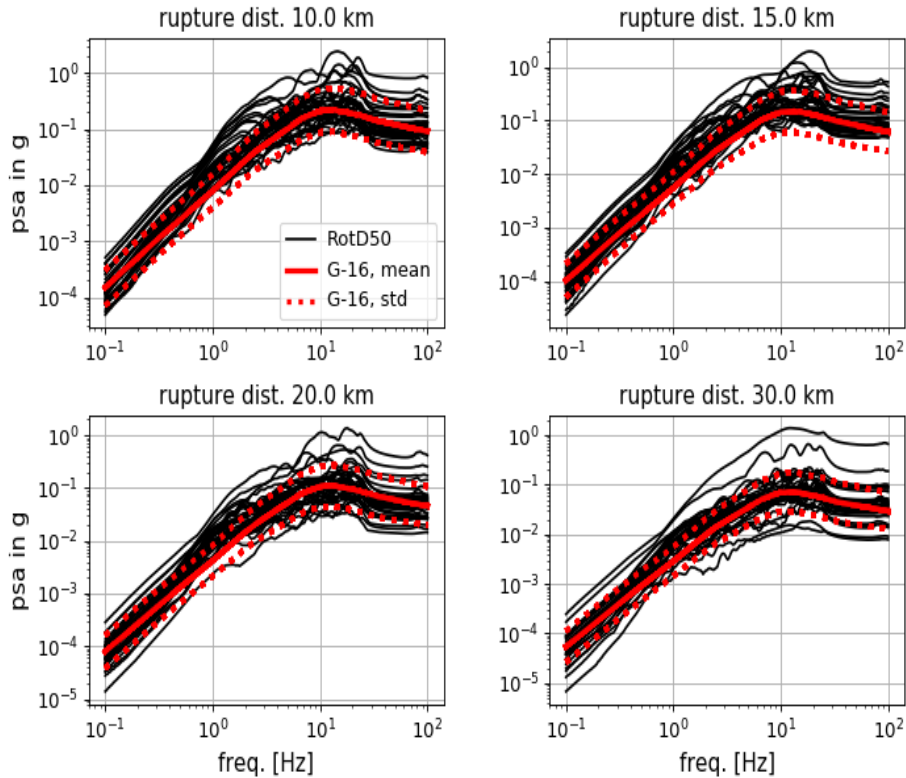


Figure 17. Comparison of spectra in black computed from the simulated ground-motion and the G-16 GMPE in red. The plot corresponds to $M_w=5.0$, all earthquake cases.

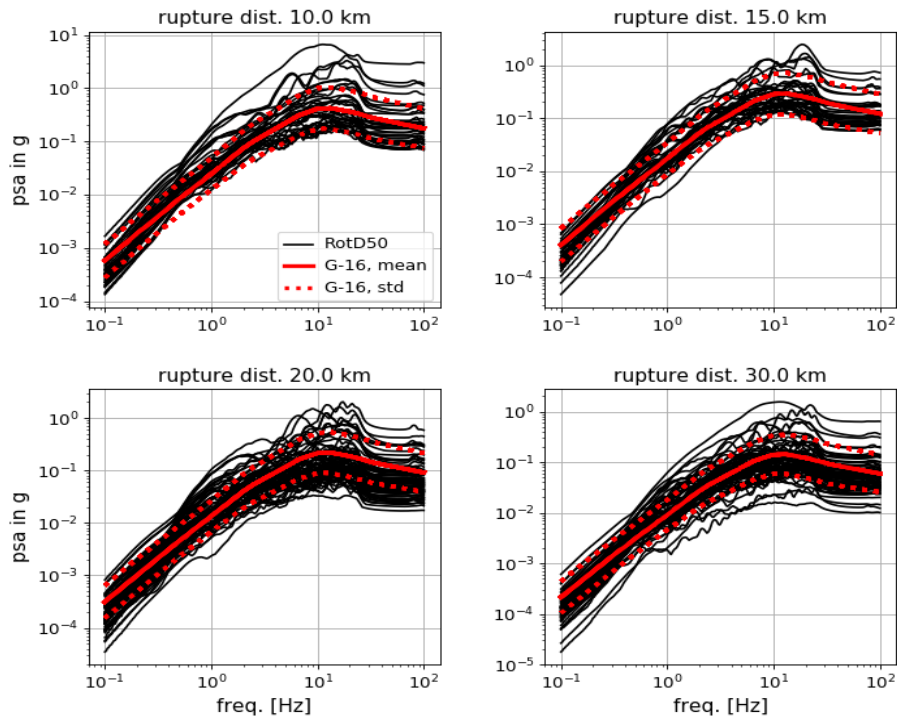


Figure 18. Comparison of spectra in black computed from the simulated ground-motion and the G-16 GMPE in red. The plot corresponds to the $M_w=5.4$ and 5.5 earthquakes.

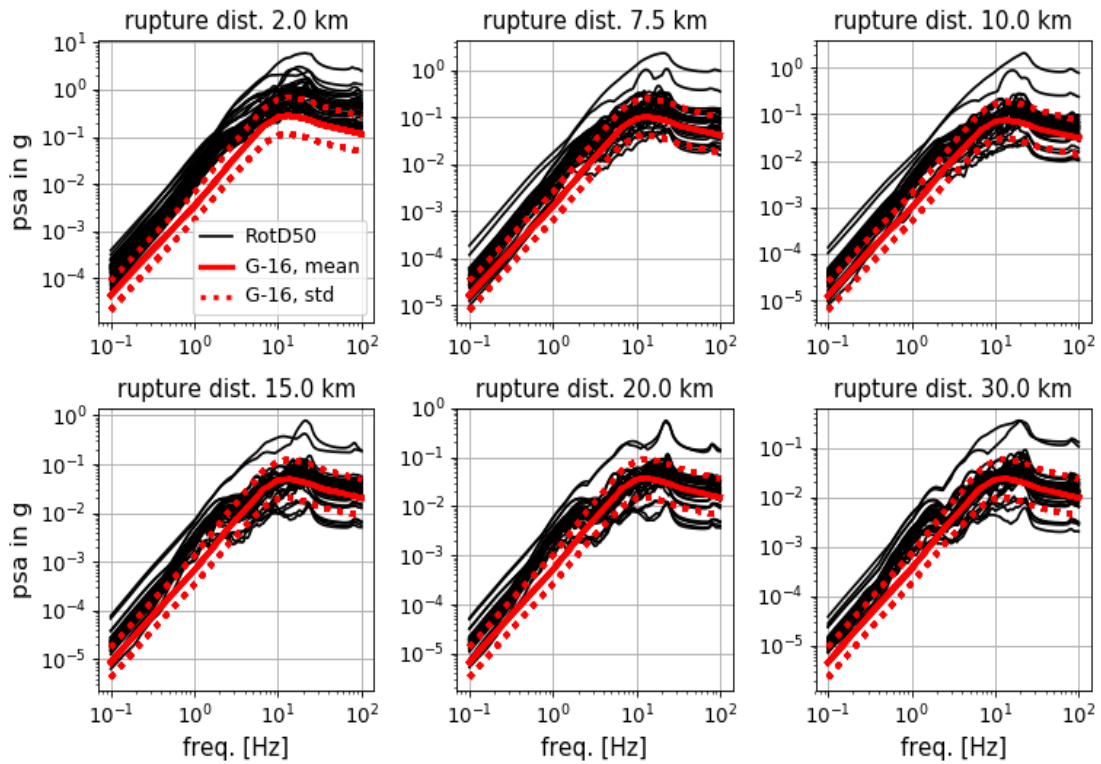


Figure 19. Comparison of spectra in black computed from the simulated ground-motion and the G-16 GMPE in red. The plot corresponds to $M_w=4.3$, hypocentre depth 2 km.

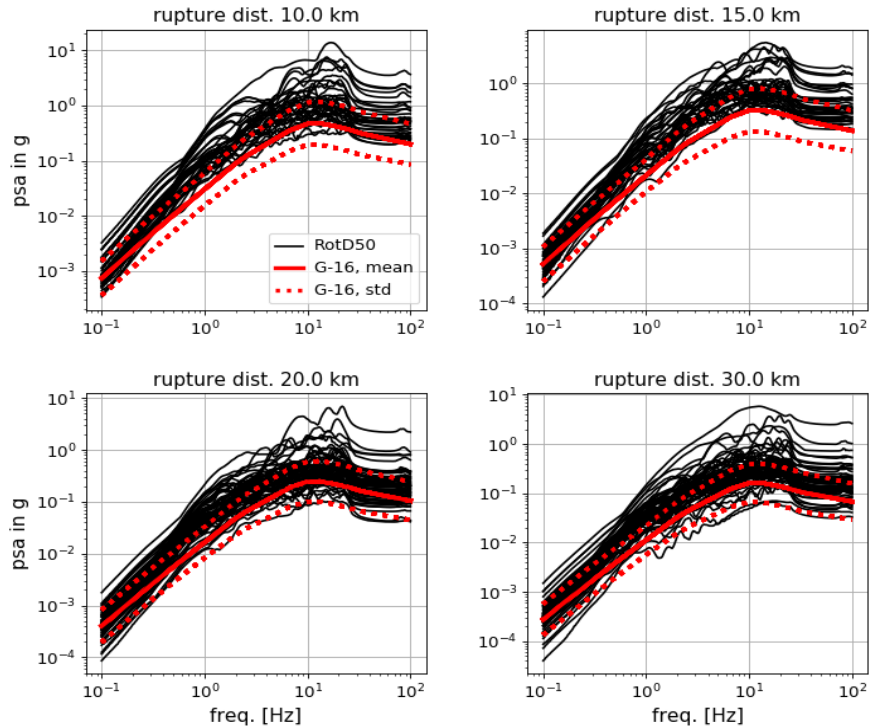


Figure 20. Comparison of spectra in black computed from the simulated ground-motion and the GMPE in red. The plot corresponds to the $M_w=5.6$ earthquakes.

5 Conclusions

The dataset of all spectra calculated in this project is in the annex of this report, as the main outcome of the project. Qualitatively, the results are in line with the expectations.

Considering the complexity of the modelled phenomena, we consider the results to be very good. The match of the peak-ground acceleration (PGA) with the chosen ground motion prediction equation (GMPE) is reasonable. As with natural recordings, the randomness of ground motions is high. However, mean PGA values align very well with the GMPE, slightly exceeding the GMPE prediction. It has to be emphasised again, that both sides of the comparison are predictions. The chosen GMPE by Graizer (2016) is an estimation of the ground motion attenuation, as are the hybrid modelling results.

The two less typical earthquake scenarios modelled by is highlight the very big differences in ground motion, which can be introduced by the parameters hidden in the GMPEs. Depth is integrated in R_{rup} , and hence it is indirectly a parameter in G-16. Still, the hypocentre depth of only 2km for the $M_w=4.3$ earthquake is not handled well by the GMPE prediction.

On the other hand, the stress-drop as parameter is completely hidden. It only influences the moment magnitude indirectly and it depends on the earthquakes selected for the calibration of the GMPE equations. Our models show the important influence of the stress drop on ground motion intensity. Hence, when adopting a GMPE to Fennoscandia one should be very careful of compatibility in magnitudes, depth distribution and stress-drops.

We propose the outputs of the hybrid modelling to be used for guiding the GMPEs for close ranges to the epicentres.

6 Future prospects

We plan to explore comparisons with other GMPEs, for instance the Varpasuo-Saari-Nikkari GMPE (Varpasuo *et al*, 2001), which has been applied for many years in Finland.

The other explored path could be to extend the frequency coverage of the models. This has not been possible before, due to the limitations of the Compsyn code. However, we are able now to split the ground motion generation modelling to parallel processing with several CPUs, decreasing the computational time from hours to minutes.

After exploring these development paths for the hybrid modelling, we consider additional parametric models. As seen in this data, less scrutinised parameters like stress-drop are significantly influencing the ground motion levels.

7 Acknowledgements

The authors express appreciation to the Finnish Radiation and Nuclear Safety Authority (STUK) and Swedish Radiation Safety Authority (SSM) for the continuous interest and support in developing and improving the hybrid modelling technique. We also thank Fennovoima for co-financing this particular project.

The authors express their gratitude to Dr. Vladimir Graizer of the United States Nuclear Regulatory Commission (USNRC), for providing in depth information about the G-16 GMPE, its strengths and limitation within the context of our work.

NKS conveys its gratitude to all organizations and persons who by means of financial support or contributions in kind have made the work presented in this report possible.

8 Disclaimer

The views expressed in this document remain the responsibility of the author(s) and do not necessarily reflect those of NKS. In particular, neither NKS nor any other organisation or body supporting NKS activities can be held responsible for the material presented in this report.

9 References

- Bizzarri, A. 2010. How to Promote Earthquake Ruptures: Different Nucleation Strategies in a Dynamic Model with Slip-Weakening Friction. *Bulletin of the Seismological Society of America* 100(3): 923-940. doi:10.1785/0120090179.
- Bizzarri, A. 2012. Rupture speed and slip velocity: What can we learn from simulated earthquakes? *Earth and Planetary Science Letters* 317: 196-203. doi:10.1016/j.epsl.2011.11.023.
- Boore, D.M., 2010. Orientation-Independent, Nongeometric-Mean Measures of Seismic Intensity from Two Horizontal Components of Motion. *Bulletin of the Seismological Society of America* 100, 1830–1835. <https://doi.org/10.1785/0120090400>
- Bödvarsson, R., Lund, B., Roberts, R., & Slunga, R. (2006). Earthquake activity in Sweden. Study in connection with a proposed nuclear waste repository in Forsmark or

- Oskarshamn. SKB Report R-06-67. Svensk Kärnbränslehantering AB (SKB), Sockholm, Sweden.
- Cundall, P.A. A computer model for simulating progressive large scale movements in blocky rock systems. In Symposium of the International Society for Rock Mechanics. Nancy, France 1971.
- Fälth, B., Hökmark, H., Lund, B., Mai, P.M., Roberts, R., and Munier, R. 2015. Simulating earthquake rupture and off-fault fracture response: Application to the safety assessment of the Swedish nuclear waste repository. *Bull. Seism. Soc. Am.* 105(1). doi:10.1785/0120140090.
- Fülöp, L., Jussila, V., Malm, M., Tiira, T., Saari, J., Li, Y., Mäntyniemi, P., Heikkinen, P., Puttonen, J., 2015. Seismic Safety of Nuclear Power Plants - Targets for Research and Education (SESA) - Final Report, in: SAFIR2014, The Finnish Research Programme on Nuclear Power Plant Safety 2011-2014, (Final Report), VTT Technology. VTT Technical Research Centre of Finland, Espoo, pp. 604–619.
- Fülöp, L., Jussila, V., Lund, B., Fälth, B., Voss, P., Puttonen, J., Saari, J., 2016. Modelling as a tool to augment ground motion data in regions of diffuse seismicity - Progress 2015. NKS Nordic Nuclear Safety Research. ISBN: 978-87-7893-448-2
- Fülöp, L., Jussila, V., Lund, B., Fälth, B., Voss, P., Puttonen, J., Saari, J., and Heikkinen, P. 2017. Modelling as a Tool to Augment Ground Motion Data in Regions of Diffuse Seismicity – Final report. NKS - Nordic Nuclear Safety Research NKS-394, Roskilde, Denmark, ISBN: 978-87-7893-481-9
- Gephart, J.W. and Forsyth, D.W. 1984. An improved method for determining the regional stress tensor using earthquake focal mechanism data: Application to the San Fernando earthquake sequence. *J. Geophys. Res.* 89: 9305-9320.
- Glamheden, R., Fredriksson, A., Röshoff, K., Karlsson, J., Hakami, H., & Christiansson, R. (2007). Rock Mechanics Forsmark. Site descriptive modelling Forsmark stage 2.2. SKB Report R-07-31. Svensk Kärnbränslehantering AB (SKB), Sockholm, Sweden.
- Goulet, C., Kishida, T., Ancheta, T., Cramer, C., Darragh, R., Silva, W., Hashash, Y., Harmon, J., Stewart, J., Wooddell, K. Youngs, R., 2014, PEER NGA-East Database, PEER 2014/17, Pacific Earthquake Engineering Research Center, Berkeley
- Grad, M., Tiira, T., ESC Working Group; The Moho depth map of the European Plate, *Geophysical Journal International*, Volume 176, Issue 1, 1 January 2009, Pages 279–292, <https://doi.org/10.1111/j.1365-246X.2008.03919.x>
- Graizer, V., 2016. Ground-Motion Prediction Equations for Central and Eastern North America. *Bulletin of the Seismological Society of America* 106, 1600–1612. <https://doi.org/10.1785/0120150374>
- Gregersen, S., Wiejacz, P., Dębski, W., Domanski, B., Assinovskaya, B., Guterch, B., Mäntyniemi, P., Nikulin, V.G., Pacesa, A., Puura, V., Aronov, A.G., Aronova, T.I., Grünthal, G., Husebye, E.S., Sliupa, S., 2007. The exceptional earthquakes in Kaliningrad district, Russia on September 21, 2004. *Physics of the Earth and Planetary Interiors* 164, 63–74. <https://doi.org/10.1016/j.pepi.2007.06.005>
- Hanks, T.C. and Kanamori, H. 1979. A moment magnitude scale. *Journal of Geophysical Research* 84(NB5): 2348-2350. doi:10.1029/JB084iB05p02348.

- Itasca. 2013. 3DEC – 3-Dimensional Distinct Element Code, User’s Guide. Itasca Consulting Group Inc., Minneapolis, USA.
- Jaeger, J.C. and Cook, N.G.W. 1979. Fundamentals of rock mechanics. Third ed. Science Paperbacks/Chapman and Hall, London, UK.
- Jussila, V., Fälth, B., Lund, B., Saari, J., Voss, P., Puttonen, J., Fülöp, L., 2017. Decreasing uncertainty in seismic hazard estimates in Fennoscandia by use of seismic source modeling. *ATS Ydintekniikka* 46, 16–22.
- Kanamori, H., & Anderson, D. L. (1975). Theoretical basis of some empirical relations in seismology. *Bulletin of the Seismological Society of America*, 65(5), 1073-1095.
- Korja, A., & Kosonen, E. (2015). Seismotectonic framework and seismic source area models in Fennoscandia, northern Europe. Report S-63. Institute of Seismology, University of Helsinki.
- Lund, B., & Zoback, M. D. (1999). Orientation and magnitude of in situ stress to 6.5 km depth in the Baltic Shield. *International Journal of Rock Mechanics and Mining Sciences*, 36, 169-190. doi:10.1016/S0148-9062(98)00183-1.
- Olson, A., Orcutt, J. and Frazier, G. (1984). The discrete wavenumber/finite element method for synthetic seismograms, *Geophys. J. R. Astron. Soc.* 77:421-460.
- Onwuemeka, J., Liu, Y., Harrington, R.M., 2018. Earthquake Stress Drop in the Charlevoix Seismic Zone, Eastern Canada. *Geophysical Research Letters* 45, 12,226-12,235. <https://doi.org/10.1029/2018GL079382>
- Posiva. (2011). Olkiluoto Site Description 2011. Posiva Report 2011-02.
- Slunga, R. S. (1991). The Baltic Shield earthquakes. *Tectonophysics*, 189, 323-331.
- Spudich, P. and Archuleta, R. (1987). Techniques for Earthquake Ground-Motion Calculation with Applications to Source Parameterization of Finite Faults. In: Bolt, B. A. (Ed.), *Seismic Strong Motion Synthetics*, Academic Press, Inc.
- Spudich, P. and Xu, L. (2003). 85.14 Software for calculating earthquake ground motions from finite faults in vertically varying media. In: William, H. K.; Lee, H. K.; Jennings, P. C. & Kisslinger, C. (Ed.), *International Handbook of Earthquake and Engineering Seismology*, Academic Press.
- Uski, M., Hyvönen, T., Korja, A., & Airo, M.-L. (2003). Focal mechanisms of three earthquakes in Finland and their relation to surface faults. *Tectonophysics*, 363, 141-157.
- Uski, M., Tiira, T., Korja, A., & Elo, S. (2006). The 2003 earthquake swarm in Anjalankoski, south-eastern Finland. *Tectonophysics*, 422, 55-69. doi:10.1016/j.tecto.2006.05.014.
- Varpasuo, P., Saari, J., Nikkari, Y., 2001. Seismic Hazard and Ground Motion for Leningrad NPP site, in: ResearchGate. Presented at the Transactions of the 16th International Conference on Structural Mechanics in Reactor Technology (SMiRT16), Washington DC, USA.
- Zoback, M.D. and Townend, J. 2001. Implications of hydrostatic pore pressures and high crustal strength for the deformation of intraplate lithosphere. *Tectonophysics* 336(1-4): 19-30.

| | |
|----------------------------------|---|
| Title | Synthetic ground motions to support the Fennoscandian GMPEs |
| Author(s) | Ludovic Fülöp ¹ , Vilho Jussila ¹ , Billy Fälth ² , Peter Voss ³ , Björn Lund ⁴ |
| Affiliation(s) | ¹ VTT Technical Research Centre of Finland Oy, ² Claytech AB, ³ Geological Survey of Denmark and Greenland (GEUS), ⁴ Uppsala University |
| ISBN | 978-87-7893-514-4 |
| Date | April 2019 |
| Project | NKS-R / SYNTAGMA |
| No. of pages | 31 |
| No. of tables | 6 |
| No. of illustrations | 20 |
| No. of references | 32 |
| Abstract max. 2000 characters | The relevance of near-field earthquakes to the safety of nuclear power plants (NPPs) in Fennoscandia is very high. De-aggregation from probabilistic seismic hazard assessment (PSHA) studies indicates that the prevailing source of hazard from ground accelerations of engineering interest is from mid-magnitude earthquakes at less than 50 km distance from the NPPs. Unfortunately, there are very few recordings of Fennoscandian earthquakes in the range of distances of this highest interest. We have developed a method to generate synthetic ground motions by physics-based modeling. Since the ground motion prediction (GMPE) is an essential part of PSHA computation we verify the simulation results with the G-16 GMPE (Graizer) developed for hard rock sites. The agreement between G-16 and our results is good at distances up to 30 km. |
| Key words | earthquake modeling, synthetic ground motions, probabilistic hazard assesment |